



### **Science Arts & Métiers (SAM)**

is an open access repository that collects the work of Arts et Métiers Institute of Technology researchers and makes it freely available over the web where possible.

This is an author-deposited version published in: <https://sam.ensam.eu>  
Handle ID: <http://hdl.handle.net/10985/19355>

#### **To cite this version :**

El-Hadi TIKARROUCHINE, Adil BENAARBIA, George CHATZIGEORGIOU, Fodil MERAGHNI - Non-linear FE2 multiscale simulation of damage, micro and macroscopic strains in polyamide 66-woven composite structures: analysis and experimental validation - Composite Structures - Vol. 255, p.112926 - 2020

Any correspondence concerning this service should be sent to the repository

Administrator : [scienceouverte@ensam.eu](mailto:scienceouverte@ensam.eu)



# Non-linear FE<sup>2</sup> multiscale simulation of damage, micro and macroscopic strains in polyamide 66-woven composite structures: analysis and experimental validation

E. Tikarrouchine<sup>a,b</sup>, A. Benaarbia<sup>a</sup>, G. Chatzigeorgiou<sup>a</sup>, F. Meraghni<sup>a,\*</sup>

<sup>a</sup>Arts et Métiers Institute of Technology, CNRS, Université de Lorraine, LEM3, F-57000 Metz, France

<sup>b</sup>Ecole Militaire Polytechnique (EMP), LDSM, BP17, Bordj El-Bahri, 16111 Alger, Algérie

## Abstract

This paper presents an experimental approach aimed at analyzing and validating a two-scale nonlinear Finite Element (FE<sup>2</sup>) simulation of a 3D composite structure. The studied composite material consists of polyamide thermoplastic matrix, exhibiting viscoelastic-viscoplastic behavior with ductile damage, reinforced by woven glass fabric whereby inelastic and anisotropic damage behavior is considered. The multiscale parallel computation is founded on the periodic homogenization at the microscopic scale, which considers the geometric description of the reinforcement's architecture and accounts for time-dependent and non-linear local behavior of each constitutive phase. For the numerical implementation at microscopic and macroscopic scales, an advanced UMAT subroutine is developed and combined with a parallelization technique in the commercial software Abaqus/Standard. The multilevel computation is achieved simultaneously at both scales (microscopic and macroscopic) through an incremental scheme. Numerical results of the FE multiscale simulation are analyzed and compared with the experimental results obtained for different stacking sequence configurations of a 3D woven composite holed plate subjected to tension. Besides the good agreement between the experimental and the predicted load-displacement global responses, the numerical simulation of the macroscopic strain fields reasonably agrees with those measured experimentally through the Digital Image Correlation (DIC) technique. Furthermore, the performance and the capabilities of the multiscale

\*Corresponding author.

Email addresses: el-hadi.tikarrouchine@ensam.eu (E. Tikarrouchine), adil.benaarbia@ensam.eu (A. Benaarbia), georges.chatzigeorgiou@ensam.eu (G. Chatzigeorgiou), fodil.meraghni@ensam.eu (F. Meraghni)

(FE<sup>2</sup>) strategy are demonstrated getting access, at the microstructure scale, to the microscopic strain fields and the spatiotemporal distributions of the internal variables as well as the damage evolution in the polymer matrix and the reinforcement (yarns).

*Keywords:* FE<sup>2</sup> method, Multi-scale FE computation, woven composite, periodic homogenization, viscoelastic-viscoplastic, damage, microstructure.

---

## 1. Introduction

Structural simulations and design of large components for industrial composite applications are computationally costly and assumed that the constitutive materials are often macroscopically homogeneous, obeying phenomenological constitutive laws. Nonetheless, the real materials are heterogeneous on a lower local scale, where it is necessary to capture the main mechanisms governing the behavior and failure. This is more evident in the case of composites whereby predicting the non-linear macro-structural response should necessarily integrate the material microstructural features. These composites are typical heterogeneous materials consisting of reinforced fiber and matrix, that exhibits anisotropic properties as a whole. In a highly competitive industrial context underpinned by considerations of high strength, ductility and durability with light weight, the use of these composites is considered an added-value technological solution for transport applications. The main advantage of these materials is their great flexibility in order to obtain a large spectrum of mechanical properties by modifying the architecture of the microstructure during the design step [Boufaïda \(2015\)](#).

Polyamide (PA6,6)-based woven fabric composites are known to have a complex behavior caused by the coupling between the periodic microstructure effects of the reinforcement and the rheological time-dependent properties of the thermoplastic matrix. In addition, these materials are extremely sensitive to environmental conditions, namely relative humidity and temperature. This dependence leads to a combination of rheology and complex degradation processes of the various constituents. The prediction of the material response of these materials at present is mainly dependent on experimental testing [Soden et al. \(1999\)](#); [Behera and Dash \(2015\)](#); [Dai et al. \(2015\)](#), because of the lack of advanced predictive computing tools and numerical simulations adapted to the weave architectures, which restricts the intensive use of these materials for structural

applications in the industries. For this reason, several authors have developed several numerical modeling methods in order to understand the behavior of these materials. For example, one can describe the overall behavior of the woven composite in a purely phenomenological aspect [Ladeveze and LeDantec \(1992\)](#); [Hochard et al. \(2001\)](#); [Puck and Schürmann \(2002\)](#); [Hochard et al. \(2006\)](#); [Ruijter \(2009\)](#); [Hochard and Thollon \(2010\)](#); [Krasnobrizha \(2015\)](#); [Krasnobrizha et al. \(2016\)](#); [Mahboob et al. \(2017\)](#); [Praud \(2018\)](#). Indeed, the effective properties of the material are calculated by modeling the overall structure, considering the material as a homogeneous without the microstructure effect. These models require a large number of parameters that have to be identified for each new material microstructure. Indeed, once the phenomenological model's parameters are identified, they are valid only for a specific configuration of the microstructure. This is a real limitation of these models, thereby disabling a structural design and microstructure optimization.

To deal with this issue, the material response of these composites can be also predicted with the use of multi-scale modelling approaches by considering the microstructure as a Representative Volume Element (RVE). These approaches describe the overall response of composite structures with taking into account the effects induced by the behavior of the various constituents of the microstructure. The modeling of these materials behavior accounting directly for the microstructural characteristics is most of the times computationally prohibited. Thus alternative techniques have been proposed based on the definition of an equivalent homogeneous medium. Among the existing theories, the periodic homogenization which is particularly adopted for composites with periodic microstructure, such as woven composites. In these theories, the heterogeneous material is replaced by an equivalent homogenized medium with an equivalent macroscopic response, in an average sense [Bensoussan et al. \(1978\)](#); [Sanchez-Palencia \(1978\)](#); [Suquet \(1987\)](#); [Allaire \(1992\)](#); [Murat and Tartar \(1997\)](#); [Chatzigeorgiou et al. \(2016\)](#). The equivalent medium plays the role of the link between the microscopic effects, induced by the different material constituents and their geometric characteristics in the microstructure, and the overall behavior of the heterogeneous material at the macroscopic scale [Chatzigeorgiou et al. \(2015\)](#); [Charalambakis et al. \(2018\)](#). In general, the resolution of such problem needs the use of numerical



approaches, mostly the Finite Element (FE) method (Chatzigeorgiou et al., 2018). Moreover, most publications in the literature on multi-scales approach using periodic homogenization concerning woven composites, describe the overall response of the RVE Carvelli and Poggi (2001); Tang and Whitcomb (2003); Angioni et al. (2011); Bednarczyk et al. (2015); Zhou et al. (2016); Wang et al. (2017); Zhou et al. (2018). However, The majority of the studies that predict the macroscopic response of composite structures with considering the microstructure effect through the  $FE^2$  scheme focus on composite reinforced with short fibers, long fibers or inclusions. Besides the macroscopic discretization, a multiscale ( $FE^2$ ) analysis of such composite structures requires a discretisation at the local scale (microscopic) of the microstructure Feyel (1999); Feyel and Chaboche (2000); Terada and Kikuchi (2001); Asada and Ohno (2007); Nezamabadi et al. (2009, 2010); Tchalla et al. (2013); Papadopoulos and Tavlaki (2016); Tikarrouchine et al. (2018). A recent work by He et al. (2020) presents a hierarchical multiscale ( $FE^2$ ) analysis of the elastic-plastic damage behavior and the failure mechanism in (3D) braided composite structures at high temperature. Xu et al. (2020) have proposed a novel data-driven multiscale finite element method for composite materials and structures. Applications of multiphysics  $FE^2$  schemes, based on the homogenization theory, concerning the same reinforcement have been developed in Sengupta et al. (2012); Javili et al. (2013); Schröder et al. (2016); Berthelsen et al. (2017); Berthelsen and Menzel (2019); Tikarrouchine et al. (2019), and for the textile composite in Rique et al. (2020).

Furthermore, a new  $FE^2$  strategy has been proposed recently for concurrent modelling. By combining the equations governing both levels of FE analyses, the strategy incorporates the two levels of simulations into one step. The latter results in a unique single system of equations Tan et al. (2020). Moreover, Rouf et al. (2018) proposed a new multiscale structural analysis using mechanics of structure genome in order to predict the properties of textile composites.

In addition, most of the works carried regarding the comparison between the numerical and experimental results for the woven composite have considered a single macroscopic material point Scida et al. (1999); Tabiei and Yi (2002); Anzelotti et al. (2008); Saleh et al. (2016).

The novelty of the present work resides in the multilevel FE analysis and its experimental validation for viscoelastic-viscoplastic damage response of thermoplastic reinforced woven

composites, taking into account the effects induced by the microstructure. In this framework, the multi-scale  $FE^2$  approach proposed in [Tikarrouchine et al. \(2018\)](#) is applied for a structural computation on a 3D polyamide reinforced by 2-2 twill weave glass woven fabric. The multilevel approach is able to i) predict the macroscopic response of the composite at any material point in the structure, taking into account the effects of the microstructure, and ii) provide the spatio-temporal evolution of damage and the strain at the micro-macro scales.

An experimental procedure was achieved in order to establish the validity and to demonstrate the performances of fully integrated multi-scale modelling approach ( $FE^2$ ) in the case of a structural computation on woven composites. The studied material consists of a polyamide 6-6 (PA66) matrix and a E-glass balanced woven reinforcement with a 2-2 twill weave pattern. The microstructure consists of a PA66 matrix represented by a viscoelastic-viscoplastic behavior with ductile damage and yarns represented by a non-linear behavior with anisotropic damage. A comparison between the experimental and numerical results was performed on a 3D holed plate subjected to a displacement-controlled monotonic tension loading at four different displacement rates. Three stacking sequence configurations of the holed composite plate have been tested, namely  $[0^0]$ ,  $[\pm 30^0]$  and  $[\pm 45^0]$ . The global response in terms of force vs. displacement and macroscopic local kinematic fields are measured experimentally using Digital Images Correlation (DIC) technique. Experimental load-displacement responses and the local macroscopic strain fields are then compared with those computed numerically through the multiscale FE simulation. It should be pointed out that this validation process of  $FE^2$  approach with experimental data has never been considered in the literature for the case of 3D woven fabric reinforced polyamide composite structures.

The layout of the present paper is as follows: in Section 2, the theoretical formulation of the homogenization theory is described as well as the principle of the scale transition between the microscopic and the macroscopic fields. The section also presents the multi-scale computational framework. In section 3, details of the geometrical characteristics of the woven composite microstructure are presented as well as the nonlinear constitutive laws of the phases (PA66 matrix and yarns). The section 4 presents the experimental procedure and the testing configurations

as well as the kinematic full-field measurement technique adopted for the validation of the  $FE^2$  approach. The section 5 is devoted to the comparison of the experimental and numerical results in terms of overall responses and macroscopic strain fields for the three studied stacking orientations. Finally in the section 6, the capabilities of the developed multiscale  $FE^2$  strategy are discussed and demonstrated through the prediction of the spatiotemporal distribution of the damage in the matrix and the yarns, the microscopic strains and the local stresses computed at the local scale.

## 2. Theoretical background: scale transition principles in composites under mechanical processes

This section presents briefly the general concepts of the periodic homogenization and its implementation into the  $FE^2$  computational framework. The full description of the methodology and the computational details are provided in [Tikarrouchine et al. \(2018\)](#).

Let's consider a structure, made by a composite material, under prescribed mechanical loading. The objective of the periodic homogenization is to define a behavior model for an equivalent homogeneous medium which, on average, behaves the same way with the composite ([Fig. 1](#)). The substitution is performed based on scale transition principles between the microscale (the unit cell) and the macroscopic structure. The equivalent medium properties are defined through a proper investigation at the microstructure level.

The periodic homogenization framework utilized in this work considers two scales: i) the macroscopic scale, representing the scale of the composite structure, whose coordinates are defined by the vector  $\bar{x}$ , and ii) the microscopic scale, representing the microstructure, whose coordinates are described with the vector  $x$ .

### 2.1. Variables and equations at the two scales

At the macroscopic level, the heterogeneous medium occupies the volume  $\bar{V}$  and is bounded by the surface  $\partial\bar{V}$  with the outward unit vector  $\bar{n}$ . Each point of the macro-structure is assigned with a position vector  $\bar{x}$  in  $\bar{V}$ . At the microscopic level, the unit cell contains information of different constituents observed at micro-scale and their geometry. Each macroscopic point  $\bar{x}$  is

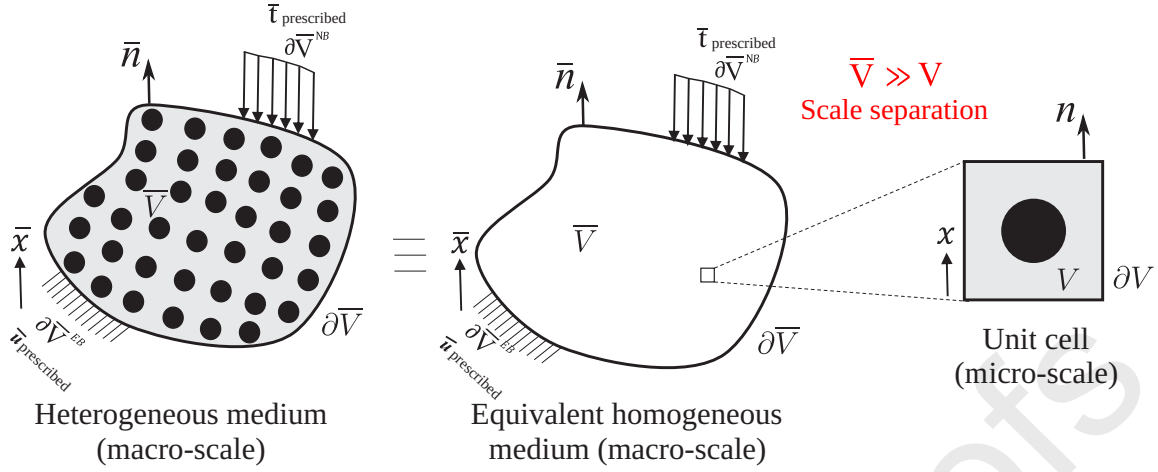


Figure 1: Schematic representation of a composite structure and substitution of the composite with an equivalent medium. The definition of the equivalent medium by periodic homogenization is valid as long as the separation between the scales (i.e.  $\bar{V} \gg V$ ) holds (Tikarrouchine et al., 2018).

assigned with a representative periodic unit cell, which occupies the volume  $V$  and is bounded by the surface  $\partial V$  with the outward unit vector  $\mathbf{n}$ .

Ignoring inertia effects, the motions of any macroscopic material point  $\bar{M}(\bar{\mathbf{x}})$  and microscopic material point  $M(\bar{\mathbf{x}}, \mathbf{x})$  are governed by the macroscopic and the microscopic equations (kinematics, equilibrium, constitutive law), respectively, which are presented in Table 1. A bar above a symbol denotes macroscopic quantity. At the two scales, the displacement vectors are  $\mathbf{u}$  and  $\bar{\mathbf{u}}$ , the strain tensors are defined as  $\boldsymbol{\varepsilon}$  and  $\bar{\boldsymbol{\varepsilon}}$  and the stress tensors are denoted by  $\boldsymbol{\sigma}$  and  $\bar{\boldsymbol{\sigma}}$ . The macroscopic body forces are denoted as  $\bar{\rho}\bar{\mathbf{b}}$ . The connection between the scales is achieved

Table 1: Macroscopic and microscopic scale governing equations (Suquet, 1987).

Equations	Macro-scale $\forall \bar{\mathbf{x}} \in \bar{V}$	Micro-scale $\forall \bar{\mathbf{x}} \in \bar{V}, \forall \mathbf{x} \in V$
Equilibrium	$\mathbf{div}(\bar{\boldsymbol{\sigma}}) + \bar{\rho}\bar{\mathbf{b}} = \mathbf{0}$	$\mathbf{div}(\boldsymbol{\sigma}) = \mathbf{0}$
Kinematics	$\bar{\boldsymbol{\varepsilon}} = \mathbf{grad}_{sym}(\bar{\mathbf{u}})$	$\boldsymbol{\varepsilon} = \mathbf{grad}_{sym}(\mathbf{u})$
Constitutive law	$\bar{\boldsymbol{\sigma}} \equiv \bar{\boldsymbol{\sigma}}(\bar{\mathbf{x}}, \bar{\boldsymbol{\varepsilon}})$	$\boldsymbol{\sigma} \equiv \boldsymbol{\sigma}(\bar{\mathbf{x}}, \mathbf{x}, \boldsymbol{\varepsilon})$
Strain energy rate	$\dot{\bar{W}}_{\varepsilon} = \bar{\boldsymbol{\sigma}} : \dot{\bar{\boldsymbol{\varepsilon}}}$	$\dot{W}_{\varepsilon} = \boldsymbol{\sigma} : \dot{\boldsymbol{\varepsilon}}$

through the usual averaging procedure of micromechanics methods. At the macroscopic position  $\bar{\mathbf{x}}$ :

$$\bar{\boldsymbol{\varepsilon}}(\bar{\mathbf{x}}) = \frac{1}{V} \int_V \boldsymbol{\varepsilon}(\bar{\mathbf{x}}, \mathbf{x}) dV, \quad \bar{\boldsymbol{\sigma}}(\bar{\mathbf{x}}) = \frac{1}{V} \int_V \boldsymbol{\sigma}(\bar{\mathbf{x}}, \mathbf{x}) dV, \quad \dot{\bar{W}}_{\varepsilon}(\bar{\mathbf{x}}) = \frac{1}{V} \int_V \dot{W}_{\varepsilon}(\bar{\mathbf{x}}, \mathbf{x}) dV. \quad (1)$$

The last relation is the well known as Hill-Mandel energy principle.

Concerning the loading conditions: i) the macroscopic scale is subjected to the external (i.e. structural) displacement and/or traction boundary conditions (Fig. 1), and ii) the microscopic scale (unit cell) is subjected to the so-called periodicity conditions, which are described by the expression

$$\mathbf{u}_i - \mathbf{u}_j = \bar{\boldsymbol{\varepsilon}} \cdot (\mathbf{x}_i - \mathbf{x}_j) \quad \forall \mathbf{x} \in \partial V, \quad (2)$$

where  $i, j$  denote a pair of opposite parallel material points at the unit cell boundary,  $\mathbf{x}_i, \mathbf{x}_j$  denote their position and  $\mathbf{u}_i, \mathbf{u}_j$  are their displacement vectors. At every macroscopic position, the macroscopic strain tensor  $\bar{\boldsymbol{\varepsilon}}$  corresponds to the attached unit cell.

For nonlinear materials, the total stress  $\boldsymbol{\sigma}$  is expressed in terms of the total strain  $\boldsymbol{\varepsilon}$  and various internal state variables, which are described by the general vector  $\mathbf{V}_k$ . The constitutive relations in such materials very seldom can be determined explicitly. For this reason incremental procedures are adopted, in which the relationship between the microscopic stress and strain is provided by the linearized expression:

$$\Delta \boldsymbol{\sigma}(\mathbf{x}) = \mathbb{D}^\varepsilon(\mathbf{x}) : \Delta \boldsymbol{\varepsilon}(\mathbf{x}) \quad \forall \mathbf{x} \in V, \quad (3)$$

where  $\mathbb{D}^\varepsilon$  is the local tangent operator tensor defined as the numerical differentiation of the stress with respect to the total strain. This tensor is obtained for each material phase from its constitutive law using appropriate techniques (for instance, a return mapping algorithm). For the macroscopic scale, the same incremental methodology based on implicit resolution scheme is used. Proper linearization permits to write the macroscopic constitutive law in the analogous incremental form:

$$\Delta \bar{\boldsymbol{\sigma}}(\bar{\mathbf{x}}) = \bar{\mathbb{D}}^\varepsilon(\bar{\mathbf{x}}) : \Delta \bar{\boldsymbol{\varepsilon}}(\bar{\mathbf{x}}) \quad \forall \bar{\mathbf{x}} \in \bar{V}, \quad (4)$$

where  $\bar{\mathbb{D}}^\varepsilon$  denotes the macroscopic tangent operator tensor. Computational details on obtaining this tensor can be found in [Tikarrouchine et al. \(2018, 2019\)](#).

## 2.2. Multi-scale computational framework: $FE^2$ approach

The previously discussed homogenization theory can be adopted for structural computations through the so-called  $FE^2$  framework. The  $FE^2$  methodology requires three main ingredients, according to [Feyel \(1999\)](#):

- (i) A geometrical description and a FE model of the unit cell, allowing to model the behavior at the microscopic scale.
- (ii) The local constitutive laws of constituents that serve to define the response of each material of the microstructure.
- (iii) Scale transition relationships that connect the microscopic and the macroscopic fields (stress and strain).

As detailed in [Tikarrouchine et al. \(2018\)](#), this approach is based on simultaneous treatment of the equations in both scales, the macroscopic scale and the unit cell. At the macroscopic scale, each material point is assigned with a unit cell. At each step of the analysis, the macroscopic structure is solved using finite element (FE) analysis for the prescribed boundary conditions. The obtained information, namely the macroscopic strain, is transmitted from every macroscopic Gauss point to the corresponding unit cell. The latter is solved under the periodicity conditions, accounting for the non-linear behavior of the material constituents of the microstructure. The transfer of the macroscopic strain to the unit cell is achieved with the help of the constraint drivers technique, which introduces six additional degrees of freedom that represent the macroscopic state of the corresponding unit cell (further details on this technique are provided in [Praud, 2018](#); [Tikarrouchine et al., 2018, 2019](#)).

The solution of the non-linear problems in any unit cell is performed through another finite element analysis, using an implicit resolution scheme based on the Newton-Raphson algorithm. Once the microscopic fields are obtained, proper averaging provides the macroscopic stress and the macroscopic tangent modulus of the corresponding macroscopic Gauss point. This information is important for the macroscopic analysis.

The adopted numerical algorithm is schematically illustrated in [Fig. 2](#). This algorithm has been developed for the study of 3D composite structures, as the one related with this work

(woven composite structure). The finite element computations have been performed using the finite element commercial software Abaqus. The connection between the unit cells and the macroscopic Gauss points is achieved through proper Meta-UMAT fortran subroutines and python scripts.

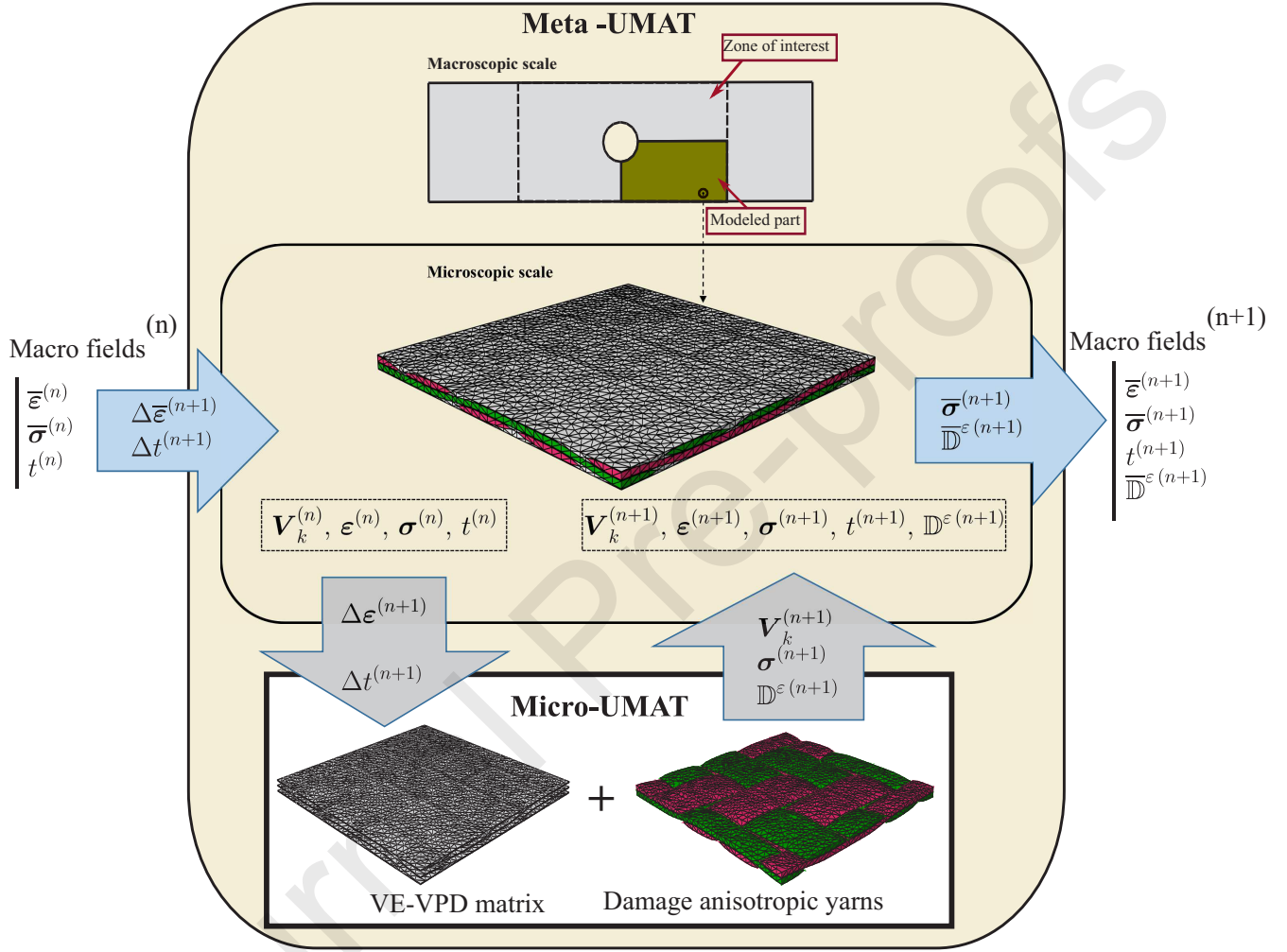


Figure 2: Algorithm of FE<sup>2</sup> methodology adopted for the studied woven composite structures. The algorithm has been adopted to the FE commercial software Abaqus with the help of specially designed fortran subroutines and python scripts.  $V_k$  represents the set of internal variables and  $t$  denotes the total time.

### 3. Microstructure of woven composite and local constitutive laws

#### 3.1. Geometrical characteristics of the microstructure

The studied composite in this work consists of glass fibers in woven formation embedded in a thermoplastic PA66 matrix material. The architecture of the woven reinforcement follows a 2-2 twill weave pattern (Fig. 3). The geometric representation of the microstructure is adopted



for FE computations through the *TexGen* software (Sherburn, 2007; Lin et al., 2011). This microstructure is defined through geometric parameters  $a$ ,  $b$ ,  $e$ ,  $L$  and  $\delta$  (Fig. 3-b), obtained by X-ray microtomography (Fig. 4 and Table 2, Praud, 2018).  $a$  and  $b$  are the cross-sections dimensions of the yarns (which are assumed of elliptic shape),  $e$  represents the thickness of the microstructure,  $L$  is the distance in the plane between the centers of the two consecutive parallel yarns and  $\delta$  is the space between two perpendicular yarns. In reality, the yarns are composed of numerous unidirectional fibers embedded in a matrix. In this work, the yarns constitutive law has been obtained via a hybrid micromechanics-phenomenological scheme, accounting for non-linear behavior and anisotropic damage (discussed later in this section).

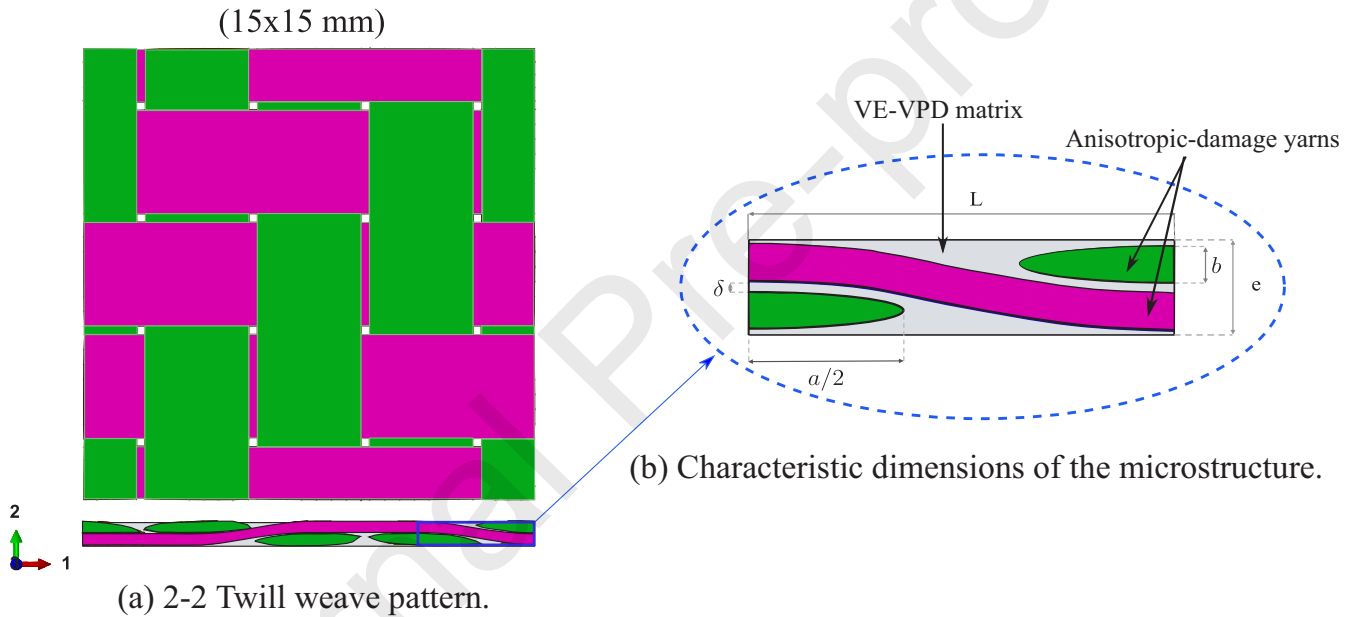
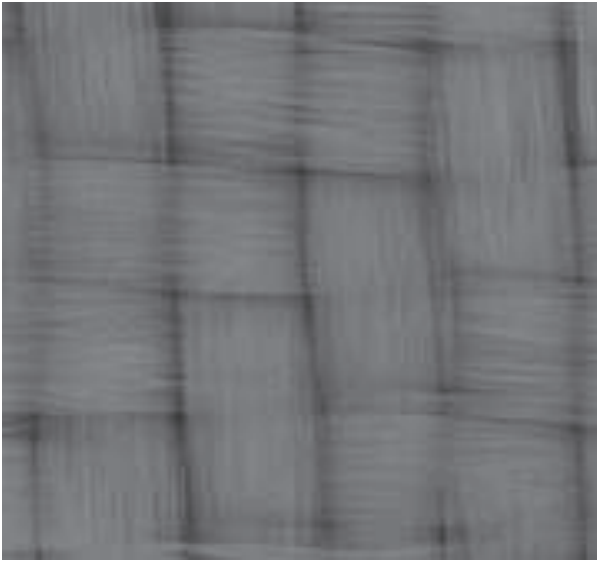


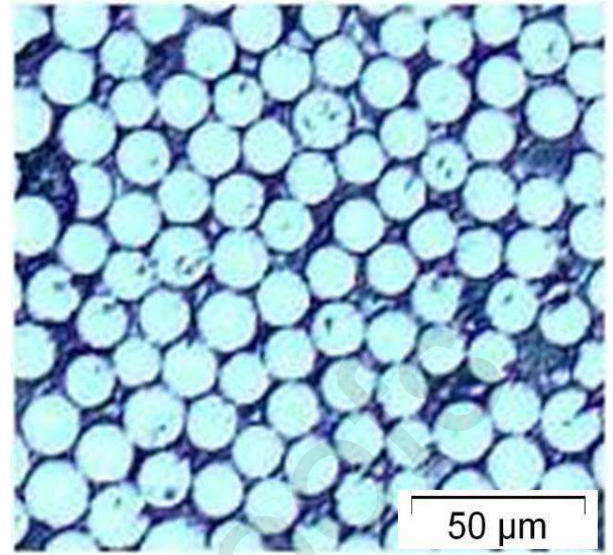
Figure 3: Geometric definition of the woven microstructure constructed via *TexGen*. The grey domain represents the matrix phase, while the pink and green domains are the warp and weft yarns, respectively.

Table 2: Characteristic dimensions of the woven microstructure of the studied composite Praud (2018).

Characteristic dimensions	$a$	$b$	$L$	$e$	$\delta$
Value (mm)	3.46	0.21	3.75	0.5	0.025

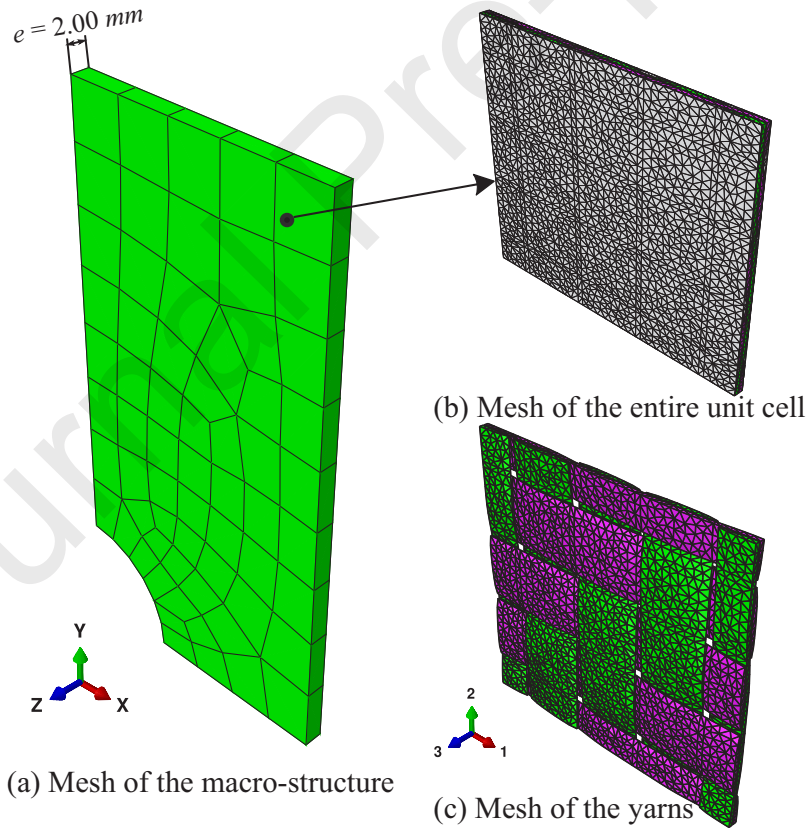


(a) Reconstruction of the woven microstructure using X-Ray microtomography with a voxel size of  $6\ \mu\text{m}$  (Pomarède et al., 2018).



(b) Fiber distribution in the yarns obtained by microtomography. The diameter of the fibers is about  $17\ \mu\text{m}$  (Praud, 2018).

Figure 4: Microstructure of the studied composite obtained through X-ray microtomography.



(a) Mesh of the macro-structure

(b) Mesh of the entire unit cell

(c) Mesh of the yarns

Figure 5: Spatial discretization of dedicated macroscopic and microscopic models for multi-scale analysis. The macroscopic FE model represents 1/4 of the Zone Of Interest (ZOI) of the plate, whereas ( $e$ ) stands for the thickness of the plate.

The volume fraction of the yarns in the unit cell is about 59%. The microtomography analyses have shown that the fibers volume fraction in the yarns is about 85%. These analyses allow to obtain the volume fraction of the fibers in the composite, which is about 50%. The X-ray microtomography analyses provide also the dimensions of the studied unit cell, which are about  $15 \text{ mm} \times 15 \text{ mm} \times 0.5 \text{ mm}$ . It is worth noticing that in such type of composites, the periodicity of the microstructure is well respected in the plane of the yarns, but it is not always satisfied in the thickness direction. In this paper, it is assumed that microstructural periodicity is satisfied in all directions.

The macro-structure under investigation is a perforated plate (plate with a hole at its center). [Fig. 5-a](#) illustrates the FE discretization of the macro-structure. The analysis is limited to the mechanically important zone and is performed on the 1/4 of the perforated plate. The FE mesh consists on 162 nodes and 64 elements of type C3D8 (8 nodes with 8 integration points, 3D solid elements for static analysis). [Figs. 5-b](#) and [5-c](#) demonstrate the FE discretization of the unit cells attached to each macroscopic integration point of the macro-model. This FE mesh consists on 8522 nodes and 40060 elements of type C3D4 (tetrahedral element with 4 node and one integration point, 3D solid element for a static analysis). To facilitate the application of the periodic boundary conditions, the mesh of the unit cell is designed to be periodic.

### 3.2. Constitutive laws

Apart from the geometrical characteristics of the unit cell, the knowledge of the behavior of each constituent is important for the accurate analysis of the studied composite. The two material constituents in this study are the PA66 matrix and the glass yarns ([Fig. 6](#)). The behavior of the PA66 matrix is described by a viscoelastic-viscoplastic behavior with ductile damage ([Praud et al., 2017a](#)), while the yarns are modeled considering inelastic behavior coupled with anisotropic damage ([Praud et al., 2017b](#)). For the reader's convenience, the essential points of the two constitutive laws are briefly discussed in the following subsections. The numerical implementation details of the two models are not discussed here and the reader is referred to the previously published works ([Praud et al., 2017a,b](#)).

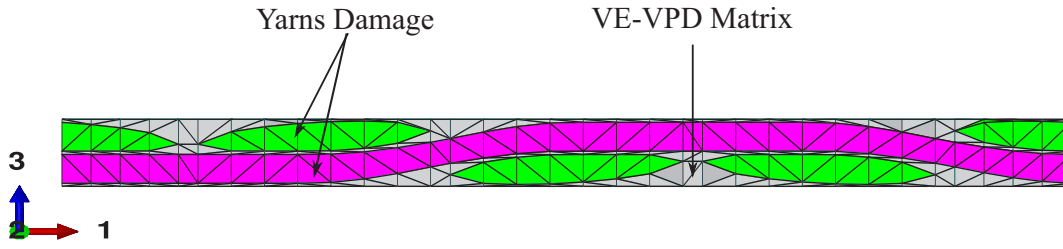


Figure 6: 2-D weaving pattern representation. The grey domain represents the matrix phase, while the pink and green domains are the warp and weft yarns, respectively.

### 3.2.1. Local constitutive model for the matrix

The constitutive law of the polymer matrix of the studied composite was developed in [Praud et al. \(2017a\)](#) using an appropriate thermodynamic framework. Semi-crystalline polymers, such as PA66, are known for their complex dissipative behavior, which depends on the time and the environmental conditions, namely the relative humidity (RH) and the temperature ([Arruda et al., 1995](#); [Launay et al., 2013](#); [Arif et al., 2014](#); [Malpot et al., 2015](#); [Praud et al., 2017a](#)). These materials are also subjected to stiffness reduction during loading caused by the damage mechanisms which are linked to the initiation, the growth and the coalescence of micro-cracks ([Nouri, 2008](#); [Nouri et al., 2009](#); [Detrez et al., 2011](#); [Margueres and Meraghni, 2013](#)).

The adopted model takes into account viscoelasticity, viscoplasticity and ductile damage in the PA66 matrix. The viscoelasticity is described through a series of Kelvin-Voigt branches, considering a differential representation. The damage is introduced via the continuous damage mechanics ("CDM") based on the well known principle of effective stress ([Lemaitre, 1985](#); [Lemaitre and Chaboche, 1990](#); [Lemaitre and Desmorat, 2005](#)).

The rheological scheme of the constitutive law is illustrated in [Fig. 7](#). It is composed of a linear elastic spring,  $N$  viscoelastic branches of Kelvin-Voigt positioned in series, and a viscoplastic branch consisting of a non-linear spring and a non-linear dash-pot assembled in parallel. The model is formulated within the framework of thermodynamics of irreversible processes ([Germain, 1973, 1982](#)). The thermodynamic framework postulates the existence of a thermodynamic potential, as a function of state variables: the total strain  $\varepsilon$ , the viscoelastic strains of the branches  $\varepsilon_{v_i}$ , the viscoplastic strain  $\varepsilon_p$ , the viscoplastic scalar  $p$  and the damage  $D$ . In this study, the

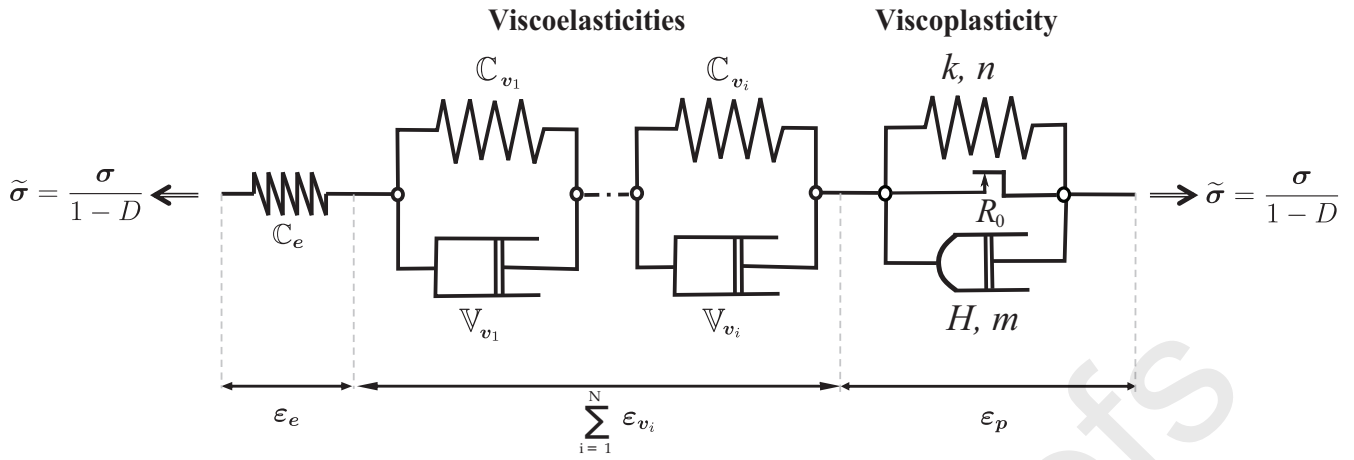


Figure 7: Rheological scheme of the PA66 thermoplastic constitutive law.

thermodynamic potential is given as the Helmholtz free energy of the form:

$$\begin{aligned} \psi(\boldsymbol{\varepsilon}, \boldsymbol{\varepsilon}_{v_i}, \boldsymbol{\varepsilon}_p, p, D) = & \frac{1}{2} \left( \boldsymbol{\varepsilon} - \sum_{i=1}^N \boldsymbol{\varepsilon}_{v_i} - \boldsymbol{\varepsilon}_p \right) : (1-D) \mathbb{C}_e : \left( \boldsymbol{\varepsilon} - \sum_{i=1}^N \boldsymbol{\varepsilon}_{v_i} - \boldsymbol{\varepsilon}_p \right) \\ & + \sum_{i=1}^N \frac{1}{2} \boldsymbol{\varepsilon}_{v_i} : (1-D) \mathbb{C}_{v_i} : \boldsymbol{\varepsilon}_{v_i} + \int_0^p R(\xi) d\xi. \end{aligned} \quad (5)$$

In the above expression,  $\mathbb{C}_e$  and  $\mathbb{C}_{v_i}$  are the initial stiffness tensors of the linear spring and the spring of the  $i^{th}$  Kelvin-Voigt branch, respectively, and  $R$  is the hardening function. The thermodynamic associated variables are obtained from the derivation of the potential with respect to the state variables. The corresponding equations are given in [Table 3](#).

From the Clausius-Duhem inequality (i.e. second principle of thermodynamics), the mechanical dissipation is always positive or null ([Grmela and Lebon, 1990](#); [Jou et al., 1999](#)). Consequently, under isothermal conditions, the dissipated energy rate is equal to the difference between the rate of the strain energy  $\dot{W}_\varepsilon$  and the rate of the stored energy  $\rho \dot{\psi}$ :

$$\dot{\Phi} = \dot{W}_\varepsilon - \rho \dot{\psi} = \sum_{i=1}^N \boldsymbol{\sigma}_{v_i} : \dot{\boldsymbol{\varepsilon}}_{v_i} + \boldsymbol{\sigma} : \dot{\boldsymbol{\varepsilon}}_p - R \dot{p} + Y \dot{D} \geq 0.$$

From the dissipated energy rate, evolution laws and activation criteria of the inelastic mechanisms can be designed. [Table 3](#) summarizes the viscoelastic, viscoplastic and the damage related evolution laws, as well as the viscoplasticity activation criterion. In this Table,  $R_0$  denotes the elasticity threshold, while  $Y$  expresses the sum of the energy density releases associated with the

Table 3: State and evolution laws of the VE-VPD model of the PA66 matrix (Praud et al., 2017a; Praud, 2018).

Observable state variable	Associated variable	
$\varepsilon$	$\sigma = \rho \frac{\partial \psi}{\partial \varepsilon} = (1 - D) \mathbb{C}_e : \left( \varepsilon - \sum_{i=1}^N \varepsilon_{v_i} - \varepsilon_p \right)$	
Internal state variables	Associated variables	Evolution laws
$\sigma_{v_i}$	$\sigma_{v_i} = -\rho \frac{\partial \psi}{\partial \varepsilon_{v_i}} = -(1 - D) \mathbb{C}_{v_i} : \varepsilon_{v_i} + \sigma$	$\dot{\varepsilon}_{v_i} = \frac{\partial \phi^*}{\partial \sigma_{v_i}} = \frac{\mathbb{V}_{v_i}^{-1}}{1 - D} : \sigma_{v_i}$
$p$	$R = \rho \frac{\partial \psi}{\partial p} = R(p)$	$\dot{p} = -\frac{\partial F}{\partial R} \dot{\lambda} = \dot{\lambda}$
$\varepsilon_p$	$-\sigma = \rho \frac{\partial \psi}{\partial \varepsilon_p}$	$\dot{\varepsilon}_p = \frac{\partial F}{\partial \sigma} \dot{\lambda} = \frac{3}{2} \frac{\text{Dev}(\sigma)}{\text{eq}(\sigma)} \frac{\dot{p}}{1 - D}$
$D$	$-Y = \rho \frac{\partial \psi}{\partial D} = Y_e + \sum_{i=1}^N Y_{v_i}$	$\dot{D} = \frac{\partial F}{\partial Y} \dot{\lambda} = \left( \frac{Y}{S} \right)^\beta \frac{\dot{p}}{1 - D}$
	Criterion	Activation VP ( $\dot{\lambda} > 0$ if $f \geq 0$ )
	$f(\sigma, R; D) = \frac{\text{eq}(\sigma)}{1 - D} - R(p) - R_0$	$\langle f \rangle_+ = Q(\dot{p})$

single spring and each Kelvin-Voigt branch,  $Y_e$  and  $Y_{v_i}$  respectively. The hardening function  $R$  is chosen here in the form of a power law. Finally,  $S$  and  $\beta$  are material parameters related to the damage. It is noted that the model considers visco-damage mechanism, thus the damage is activated simultaneously with the viscoplasticity (Praud et al., 2017a; Praud, 2018).

The material parameters of the matrix constitutive laws have been identified in the work of Praud (2018) from experiments directly performed on the unfilled polyamide 6-6 for a humidity rate of RH50 %. These parameters are summarized in Table 4.

### 3.2.2. Local constitutive model for the yarns

Concerning the constitutive law of the yarns, an anisotropic damage model coupled with inelastic behavior has been chosen (Praud et al., 2017b). The yarns are composed of numerous unidirectionally oriented fibers embedded in the matrix material. Their overall response can be considered as equivalent to that of a unidirectional composite. The utilized constitutive law is based on a hybrid micromechanical-phenomenological formulation (Guillaume, 2008;



Table 4: Material parameters for PA66 matrix at RH50 % (Praud, 2018).

Mechanisms			Parameters	value	unit
VE	Elastic spring	Young modulus	$E$	2731	MPa
		Poisson ratio	$\nu$	0.3	-
	1 <sup>st</sup> KV	Elastic modulus	$E_{v_1}$	8766	MPa
		Viscosity	$\eta_{v_1}$	1395	MPa.s
		Characteristic time	$\tau_{v_1}$	0.16	s
	2 <sup>nd</sup> KV	Elastic modulus	$E_{v_2}$	13754	MPa
		Viscosity	$\eta_{v_2}$	165601	MPa.s
		Characteristic time	$\tau_{v_2}$	12.04	s
	3 <sup>rd</sup> KV	Elastic modulus	$E_{v_3}$	15010	MPa
		Viscosity	$\eta_{v_3}$	457955	MPa.s
		Characteristic time	$\tau_{v_3}$	30.51	s
	4 <sup>th</sup> KV	Elastic modulus	$E_{v_4}$	11634	MPa
		Viscosity	$\eta_{v_4}$	1307516	MPa.s
		Characteristic time	$\tau_{v_4}$	112.39	s
VP-D		Yield threshold	$R_0$	4.86	MPa
		Isotropic hardening Coeff.	$K$	1304.33	MPa
		Isotropic hardening Exp.	$n$	0.674	
		VP resistance	$H$	47.35	MPa.s <sup>m</sup>
		VP Exp.	$m$	0.068	-
		Damage Coeff.	$S$	21.607	MPa
		Damage Exp.	$\beta$	-1.105	-

Zhu et al., 2011; Qi et al., 2016). This model takes into account the anisotropic damage in unidirectional composites, as well as the permanent inelastic strains imposed by non-closure of the micro-cracks.

The damage is introduced through a micromechanical description of a representative volume element (RVE) which contains micro-cracks. The stiffness reduction induced by the presence of these cracks is obtained through the Mori-Tanaka approach (Mori and Tanaka, 1973), by introducing a micro-cracks density  $\gamma_c$  in the RVE of the yarns. This stiffness reduction is represented by a fourth-order tensor  $\mathbb{D}(\gamma_c)$  that gradually reduces the initial transverse isotropic



stiffness tensor  $\mathbb{C}_0$  of the undamaged unidirectional composite material, as shown in Fig. 8.

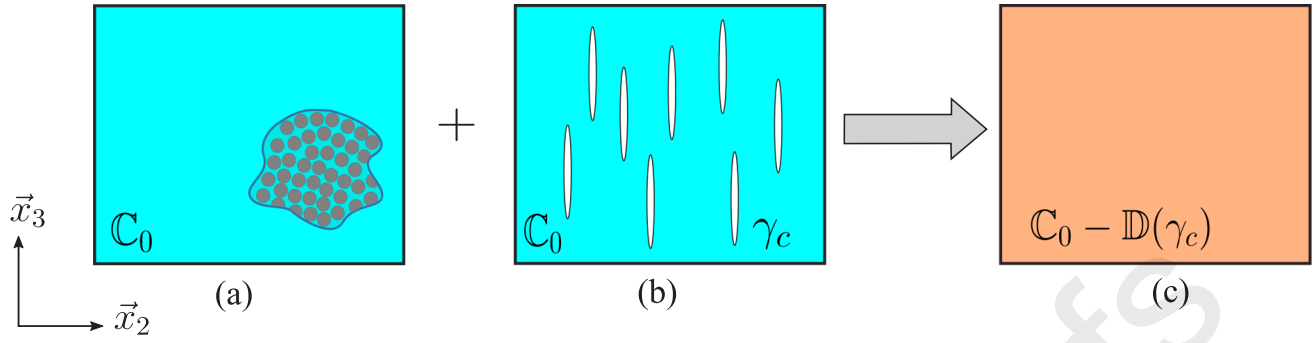


Figure 8: Damage assessment using mean field homogenization approach for the yarns constitutive law: (a) Initial state of the transverse isotropic unidirectional material. (b) Introduction of micro-cracks density  $\gamma_c$  in the RVE. (c) Evaluation of the stiffness reduction induced by  $\gamma_c$  by homogenization (Praud, 2018).

In these materials, the anisotropic damage is often accompanied by permanent inelastic strains (here denoted as  $\varepsilon_{ir}$ ), caused by non-closure effect of the micro-cracks (Ladeveze and LeDantec, 1992; Boubakar et al., 2002; Praud, 2018; Praud et al., 2017b). As a consequence, the total strain in the yarns phase is expressed as the sum of the elastic strain,  $\varepsilon_e$ , and the inelastic strain,  $\varepsilon_{ir}$ ,

$$\varepsilon = \varepsilon_e + \varepsilon_{ir}. \quad (6)$$

The overall behavior of the yarns is described by the following Helmholtz free energy potential:

$$\rho\psi(\varepsilon, \varepsilon_{ir}, \gamma_c) = \frac{1}{2} (\varepsilon - \varepsilon_{ir}) : (\mathbb{C}_0 - \mathbb{D}(\gamma_c)) : (\varepsilon - \varepsilon_{ir}). \quad (7)$$

The associated variables related to the yarn phase are given by

$$\sigma = \rho \frac{\partial \psi}{\partial \varepsilon}, \quad -\sigma = \rho \frac{\partial \psi}{\partial \varepsilon_{ir}}, \quad Y_c = -\rho \frac{\partial \psi}{\partial \gamma_c}, \quad (8)$$

where  $\sigma$  denotes the total stress and  $Y_c$  is the energy density release. Similarly to the case of the matrix constitutive law, the second principle of thermodynamics enforces the mechanical dissipation to be always positive or null. This dissipation is given by the difference between the

rate of the strain energy  $\dot{W}_\varepsilon$  and the rate of the stored energy  $\rho\dot{\psi}$ ,

$$\begin{aligned}\dot{\Phi} &= \dot{W}_\varepsilon - \rho\dot{\psi} \\ &= \boldsymbol{\sigma} : \dot{\boldsymbol{\varepsilon}} - \rho \left( \frac{\partial \psi}{\partial \boldsymbol{\varepsilon}} : \dot{\boldsymbol{\varepsilon}} + \frac{\partial \psi}{\partial \boldsymbol{\varepsilon}_{ir}} : \dot{\boldsymbol{\varepsilon}}_{ir} + \frac{\partial \psi}{\partial \gamma_c} \dot{\gamma}_c \right) \\ &= \boldsymbol{\sigma} : \dot{\boldsymbol{\varepsilon}}_{ir} + Y_c \dot{\gamma}_c \geq 0.\end{aligned}\tag{9}$$

The evolution laws are obtained from the above dissipation via an appropriate potential. Further details about this model can be found in [Praud et al. \(2017b\)](#). A summary of the thermodynamically implicated variables, the evolution laws, the micro-mechanically related fields and the damage activation criterion are provided in [Table 5](#). In this Table,  $\boldsymbol{\varepsilon}_0$  and  $\boldsymbol{\sigma}_0$  are the local strain and stress respectively in the virgin, i.e. undamaged, part of the material, connected with the relation  $\boldsymbol{\sigma}_0 = \mathbb{C}_0 : \boldsymbol{\varepsilon}_0$ . Moreover,  $\mathbb{A}_0(\gamma_c)$  is the strain localization tensor in the virgin part of the material, calculated through the Mori-Tanaka scheme [Mori and Tanaka \(1973\)](#).  $H_c$  is the anisotropic quadratic interaction criterion, in which the fourth order tensor  $\mathbb{H}$  is structured in a way that  $H_c$  stays sensitive only to the components 22 and 12 of  $\boldsymbol{\sigma}_0$ .

It is important to be noted that in this constitutive law, the viscoelastic response of the matrix inside the yarns is ignored. This simplification is motivated by the fact that the volume fraction of the fibers in the yarns is very high (about 85%), reducing significantly the time dependent effects of the matrix in the yarns.

Since it is impossible to separate the yarns from the matrix and perform mechanical tests directly on them, the material properties of the former can be identified only with inverse engineering from tests in composite specimens. [Praud \(2018\)](#) has performed an experimental campaign using quasi-static tests and the obtained parameters for the yarns are summarized in [Table 6](#).

Table 5: Summary of constitutive equations of the yarns (Praud et al., 2017b).

Observable state variable	Associated variable	
$\varepsilon$	$\sigma = \rho \frac{\partial \psi}{\partial \varepsilon} = [\mathbb{C}_0 - \mathbb{D}(\gamma_c)] : (\varepsilon - \varepsilon_{ir})$	
Internal state variables	Associated variables	Evolution laws
$\varepsilon_{ir}$	$-\sigma = \rho \frac{\partial \psi}{\partial \varepsilon_{ir}}$	$\dot{\varepsilon}_{ir} = \frac{\partial F}{\partial \sigma} \dot{\lambda} = \Lambda(\sigma) \gamma_c$
$\gamma_c$	$-Y_c = \rho \frac{\partial \psi}{\partial \gamma_c}$	$\dot{\gamma}_c = \frac{\partial F}{\partial Y_c} \dot{\lambda} = \dot{\lambda}$
Micro-mechanical variables	Local mean strain and stress in the virgin part of the material	
$\varepsilon_0$	$\varepsilon_0 = \mathbb{A}_0(\gamma_c) : (\varepsilon - \varepsilon_{ir})$	
$\sigma_0$	$\sigma_0 = \mathbb{C}_0 : \mathbb{A}_0(\gamma_c) : (\varepsilon - \varepsilon_{ir})$	
	Criterion	Activation ( $\dot{\lambda} > 0$ if $H_c = \sup(H_c)$ )
	$H_c = \sqrt{\sigma_0 : \mathbb{H} : \sigma_0}$	$\gamma_c = g(\sup(H_c))$

## 4. Experimental approach

### 4.1. Test specimens

The experiments were carried out using plates of PA66-based woven composites. Five test specimens were cut from these plates using a water jet cutting machine with suitable size and shape for the clamping jaws of the loading machine. The dimensions of the machined specimens are schematically presented in Fig. 9. The gage part contains 9 RVEs in-length and 4 RVEs in-width, with a RVE size of about 15 mm<sup>2</sup>.

After manufacturing, the samples were conditioned in a climatic chamber under an air containing 50% of relative humidity at 65°C. The conditioning process was continued until the water concentration was relatively homogeneous throughout the specimen ( $\sim 2.8\%$ ). All specimens were sealed prior to testing to maintain a controlled uniform humidity.

Laminated perforated plates having symmetric and balanced stacking sequences were investigated in the current work. The thickness of a single layer was about 0.5 mm, making a total

Table 6: Material parameters of the yarns (Praud, 2018).

	Parameters	value	unit
Transversely isotropic stiffness tensor (non-null components)	$C_{0111}$	65822	MPa
	$C_{0112} = C_{0113}$	7041	MPa
	$C_{0222} = C_{0333}$	23947	MPa
	$C_{0223}$	6971	MPa
	$C_{01212} = C_{01313}$	8661	MPa
	$C_{02323} = \frac{1}{2} (C_{0222} - C_{0223})$	8488	MPa
Pure transverse tension threshold	$R_{22}$	20.0	MPa
Pure in-plane shear threshold	$R_{12}$	7.5	MPa
1 <sup>st</sup> Weibull law parameter	$S$	12.3	-
2 <sup>nd</sup> Weibull law parameter	$\beta$	2.75	-
Micro-cracks saturation	$\gamma_c^\infty$	0.025	-
Inelasticity in transverse tension	$a_{22}$	3.6	-
Inelasticity for shear 12	$a_{12}$	2.15	-

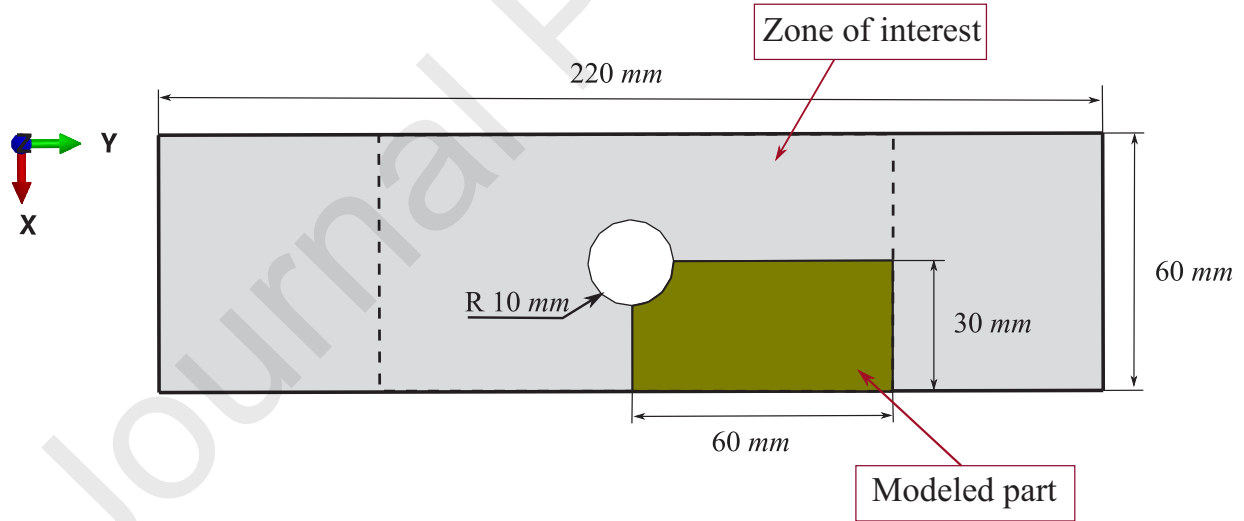


Figure 9: Geometry of the specimens used for the experiments showing the relative position of the interested part as well as the modeled part.

thickness of 2.0 mm for the whole laminated specimens. Three stacking sequence configurations were considered: samples oriented at 30°, 45° and 90° from the warp direction (Fig. 10).

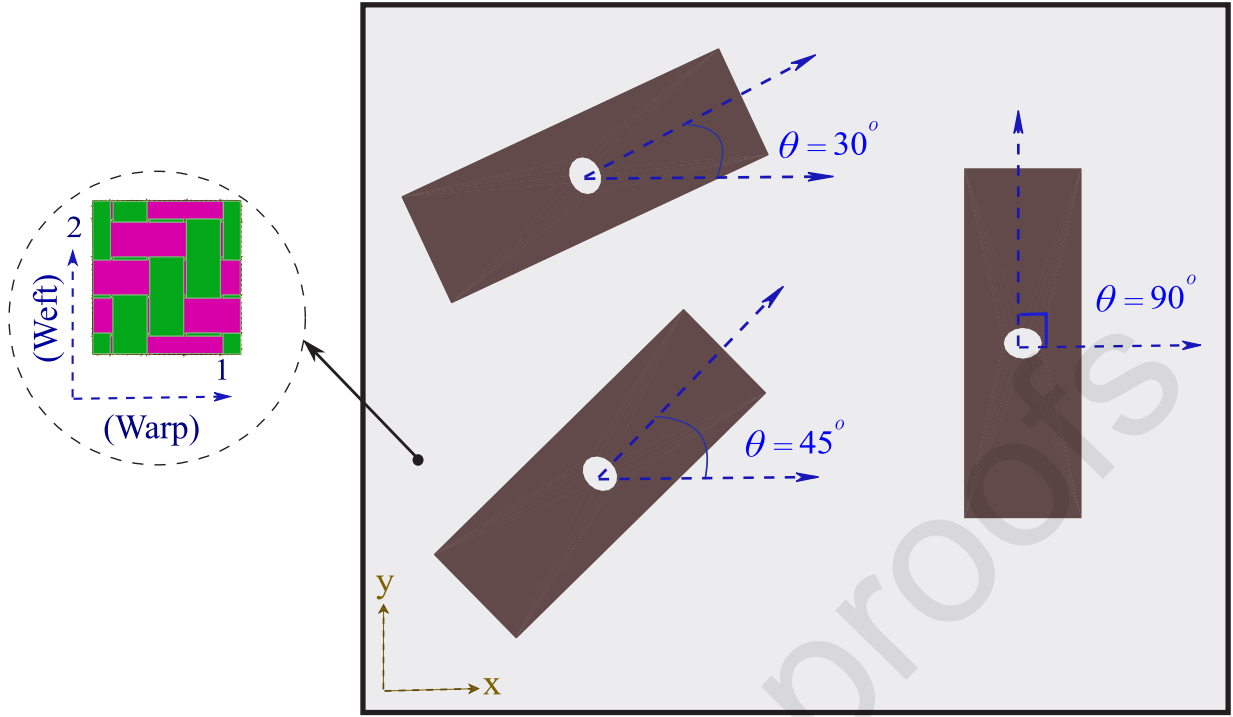


Figure 10: Sketch of composite sample configurations used for the experiments.

#### 4.2. Experimental setup and data processing

Monotonic tensile tests at different rates ( $\dot{u}_y = 0.024 \text{ mm.s}^{-1}$ ,  $\dot{u}_y = 0.033 \text{ mm.s}^{-1}$ ,  $\dot{u}_y = 0.24 \text{ mm.s}^{-1}$  and  $\dot{u}_y = 0.33 \text{ mm.s}^{-1}$ ) have been performed at 23°C room temperature using a MTS 647 hydraulic testing machine (Fig. 11). The kinematic images were recorded using a visible charge-coupled device (CCD) camera. This camera is equipped with a 2400 x 2000 pixel CCD sensor with an acquisition rate of approximately 30 images per second. Random pattern was achieved by spraying the specimen surface with a painted speckle pattern. A cold light source was used to obtain well-illuminated and high-contrast images.

In the current work, two images per seconds were recorded for the high-rate tests ( $\dot{u}_y = 0.24 \text{ mm.s}^{-1}$  and  $\dot{u}_y = 0.33 \text{ mm.s}^{-1}$ ). For the low-rate tests ( $\dot{u}_y = 0.024 \text{ mm.s}^{-1}$  and  $\dot{u}_y = 0.033 \text{ mm.s}^{-1}$ ), the acquisition frequency was set at 1 image per second. Displacement fields were thus determined using the VIC2D image correlation software (Meraghni et al., 2011; Chemisky et al., 2015). Since the experimental data were inherently noisy, appropriate spatial smoothing methods were employed to reduce the effect of noise on the strain estimate.

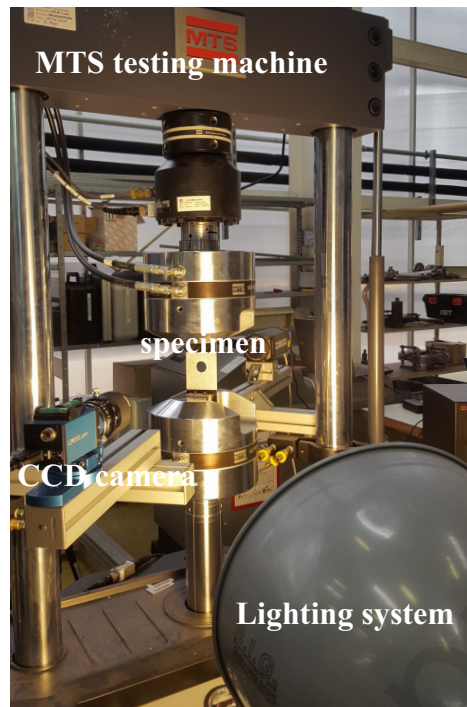


Figure 11: Experimental setup showing the CCD camera used for recording displacement surface fields.

## 5. Experimental results and comparison with the FE<sup>2</sup> approach

In the following, the overall and local responses of the investigated woven composite under the three studied configurations are compared with the numerical results computed using the FE<sup>2</sup> approach.

### 5.1. Overall mechanical response

#### 5.1.1. $\pm 90$ woven composite

The  $\pm 90$  woven composite was first subjected to 0.024 and 0.24 mm.s<sup>-1</sup> monotonic tensile test till macroscopic fracture. Fig. 12 presents the experimental and numerical macroscopic response (force in kN versus displacement in mm) of the composite. Generally speaking, the results show good correlation between both responses. The corresponding error at  $t_1$ ,  $t_2$  and  $t_3$  is given in Table 7 for both loading rates. The response of the composite is quasi-elastic till 7.5 kN without significant rate effect. This can be attributed to the direction of the loading; the load is mainly carried by the weft yarns in their longitudinal direction, which behave elastically with an important stiffness.

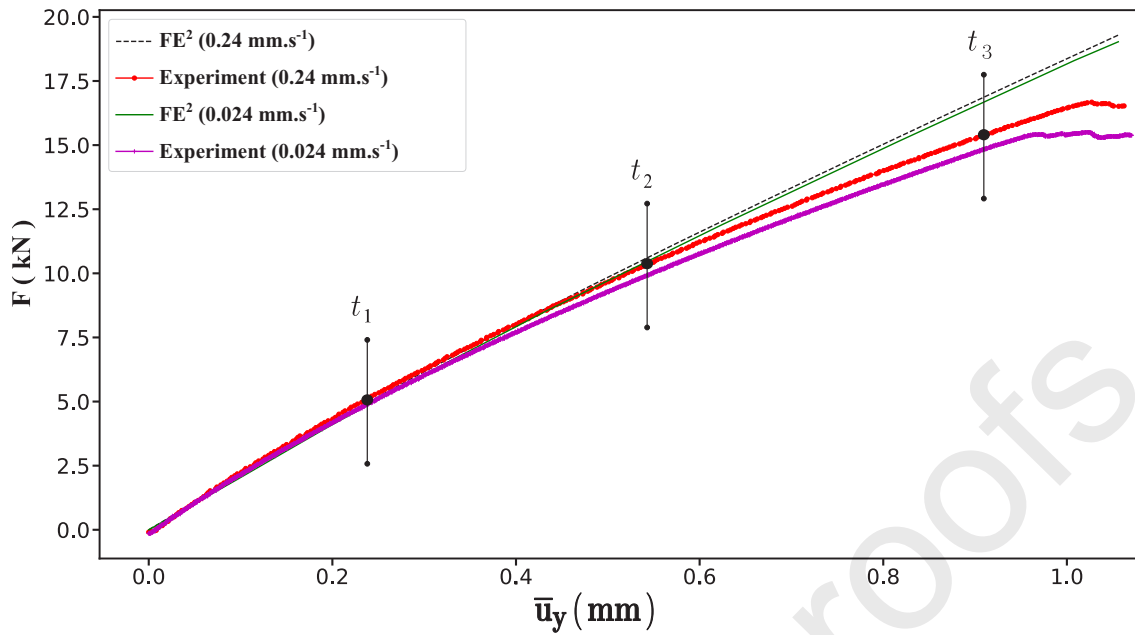


Figure 12: Macroscopic responses of the studied composite for the  $\pm 90$  stacking sequence under both loading rates  $0.024$  and  $0.24 \text{ mm.s}^{-1}$ . Comparison between DIC and  $\text{FE}^2$  approaches.

Table 7: Error estimate between both DIC and  $\text{FE}^2$  responses for the  $\pm 90$  configuration.

$\dot{u}_y \text{ (mm.s}^{-1}\text{)}$	$t_1 = 0.5 \text{ s}$	$t_2 = 1.1 \text{ s}$	$t_3 = 1.8 \text{ s}$
0.24	0.8%	3%	8%
$\dot{u}_y \text{ (mm.s}^{-1}\text{)}$	$t_1 = 5 \text{ s}$	$t_2 = 11 \text{ s}$	$t_3 = 18 \text{ s}$
0.024	0.6%	3.8%	11%

It is worth mentioning that due to the balanced nature of the woven structure,  $90$  degrees configuration (equivalent to  $0$  degrees configuration) presents weak nonlinear response and becomes quite insensitive to the loading rate. The choice of low rates for this configuration is motivated by the need to avoid rapid brittle failure compared to the responses exhibited by  $45$  and  $30$  degrees configurations.

#### 5.1.2. $\pm 45$ woven composite

The  $\pm 45$  woven composite was subjected to  $0.033$  and  $0.33 \text{ mm.s}^{-1}$  monotonic tensile test until the macroscopic fracture. Fig. 13 presents the experimental and numerical macroscopic response of the composite for both displacement rates. As illustrated in this figure, the mechanical response computed through the proposed multi-scale approach is over-estimated. The



associated error between DIC and  $FE^2$  results is given in Table 8. The mechanical response of the  $\pm 45$  composite shows a more pronounced nonlinear behaviour compared to that of the  $\pm 90$  configuration. This non-linearity can be attributed to i) the rheology of the thermoplastic matrix, ii) its ductile damage and/or iii) the degradation in the yarns (transverse cracks).

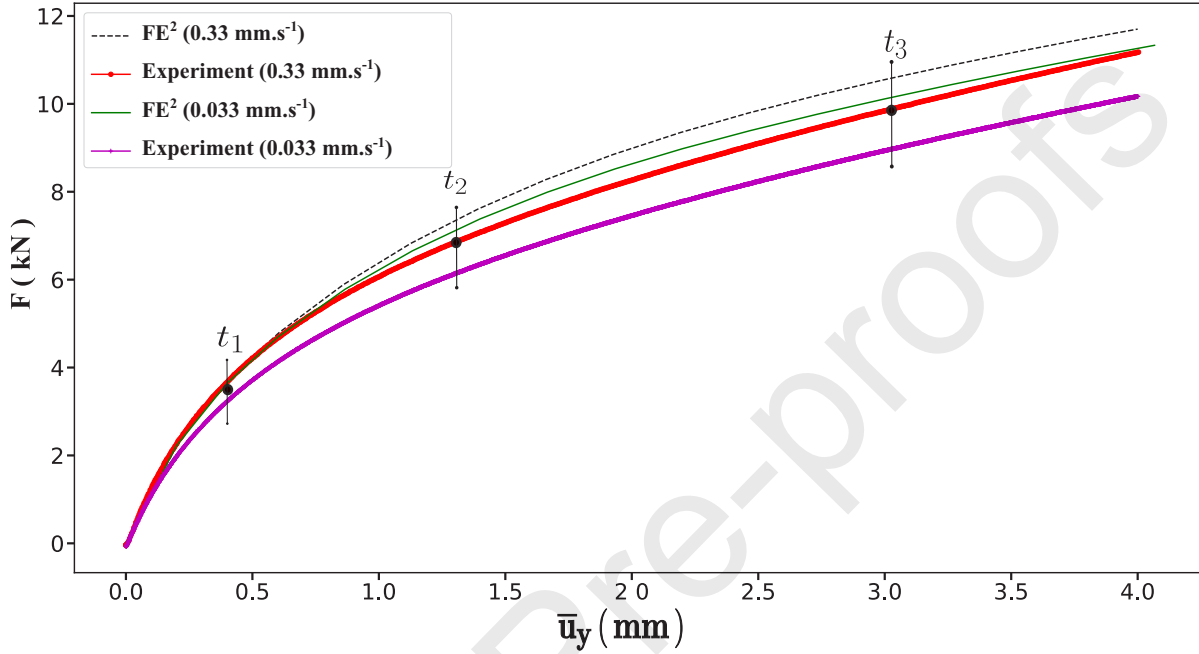


Figure 13: Macroscopic responses of the studied composite for the  $\pm 45$  stacking sequence under both loading rates 0.033 and 0.33  $\text{mm.s}^{-1}$ . Comparison between DIC and  $FE^2$  approaches.

Table 8: Error estimate between both DIC and  $FE^2$  responses for the  $\pm 45$  configuration.

$\dot{\bar{u}}_y \text{ (mm.s}^{-1}\text{)}$	$t_1 = 0.3 \text{ s}$	$t_2 = 2.1 \text{ s}$	$t_3 = 4.5 \text{ s}$
0.33	0.65%	6.4%	7.3%
$\dot{\bar{u}}_y \text{ (mm.s}^{-1}\text{)}$	$t_1 = 3 \text{ s}$	$t_2 = 21 \text{ s}$	$t_3 = 45 \text{ s}$
0.033	5%	12%	13.4%

### 5.1.3. $\pm 30$ woven composite

Fig. 14 shows the experimental versus  $FE^2$  macroscopic responses of the  $\pm 30$  woven composite subjected to both 0.033 and 0.33  $\text{mm.s}^{-1}$  loading rates. It can be seen from the figure that the multi-scale model captures well the macroscopic experimental responses till  $t_1$  and starts to over-estimate the structure's behaviour when reaching  $t_2$  with an estimated error of 18% at  $t_3$ , as reported in Table 9.

The global behaviour of the  $\pm 30$  composite presents also a non-linear response. This response can be attributed to either the rheology of the PA66 matrix and/or the degradation in the yarns caused by the presence of the micro-cracks. It is pointed out that at lower loading rates, the 30 and 45 degrees configurations have more pronounced nonlinearity due to the high viscoelastic-viscoplastic effects. For increased loading rates the composite's behavior becomes more rigid. Since the FE homogenization results present always stiffer response than the experimental findings, one can expect that the error will decrease when the loading rate increases, as shown in Tables 8 and 9. The difference in the overall responses of all composite configurations highlights the strong anisotropy of the studied material induced by the architecture of the woven microstructure.

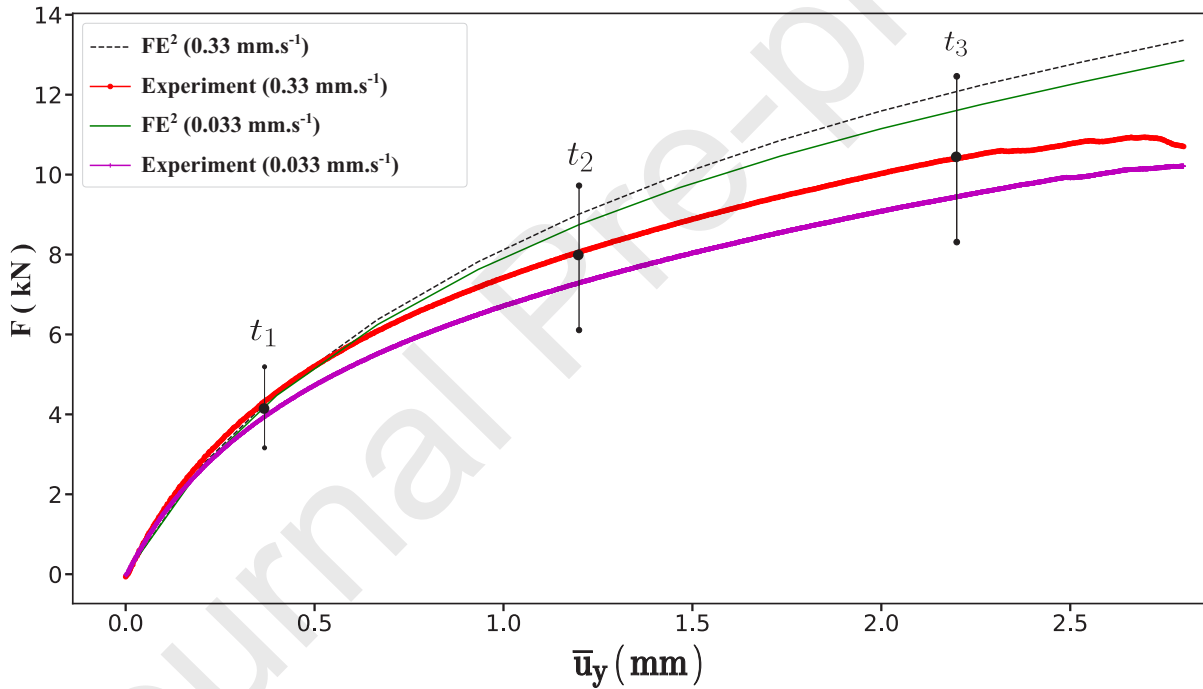


Figure 14: Macroscopic responses of the studied composite for the  $\pm 30$  stacking sequence under both loading rates 0.033 and 0.33  $\text{mm.s}^{-1}$ . Comparison between DIC and  $\text{FE}^2$  approaches.

Table 9: Error estimate between both DIC and  $\text{FE}^2$  responses for the  $\pm 30$  configuration.

$\dot{u}_y$ ( $\text{mm.s}^{-1}$ )	$t_1 = 0.6 \text{ s}$	$t_2 = 2.2 \text{ s}$	$t_3 = 3.2 \text{ s}$
0.33	0.59%	12%	16%
$\dot{u}_y$ ( $\text{mm.s}^{-1}$ )	$t_1 = 6 \text{ s}$	$t_2 = 22 \text{ s}$	$t_3 = 32 \text{ s}$
0.033	5.6%	15.6%	18.3%

## 5.2. Local mechanical response

### 5.2.1. $\pm 90$ woven composite

The kinematic assessments are analyzed in terms of engineering strain components. Three strain fields regularly captured throughout the test for three strain components ( $\bar{\epsilon}_{22}$ ,  $\bar{\epsilon}_{11}$  and  $\bar{\epsilon}_{12}$  in Figs. 15, 16 and 17, respectively) are compared with those obtained by the FE<sup>2</sup> calculation at the area of interest in the perforated plate. The values of the featured strain components are depicted and graduated on a colorbar. Generally speaking, the kinematic patterns indicate a gradual development of strain localization zones. These are clearly visible for all strain components. The spatio-temporal distributions for both longitudinal and transverse fields (Figs. 15, 16) are very comparative for both DIC and FE<sup>2</sup> simulation. Due to the anti-symmetry in the 12 direction, the comparison is restrained in the quarter of the discretized perforated plate for the shear component. Fig. 17 demonstrates a good correlation between the shear strain,  $\bar{\epsilon}_{12}$ , measured by both DIC and the FE<sup>2</sup> approach at the three considered analysis times ( $t_1$ ,  $t_2$  and  $t_3$ ). These results clearly illustrate that the proposed FE<sup>2</sup> approach, based upon microstructural effects, describes well the response of the composite material in the specific structural calculations. It is pointed out that, for sake of manuscript conciseness, the microstructure responses are presented only for the larger loading rates.

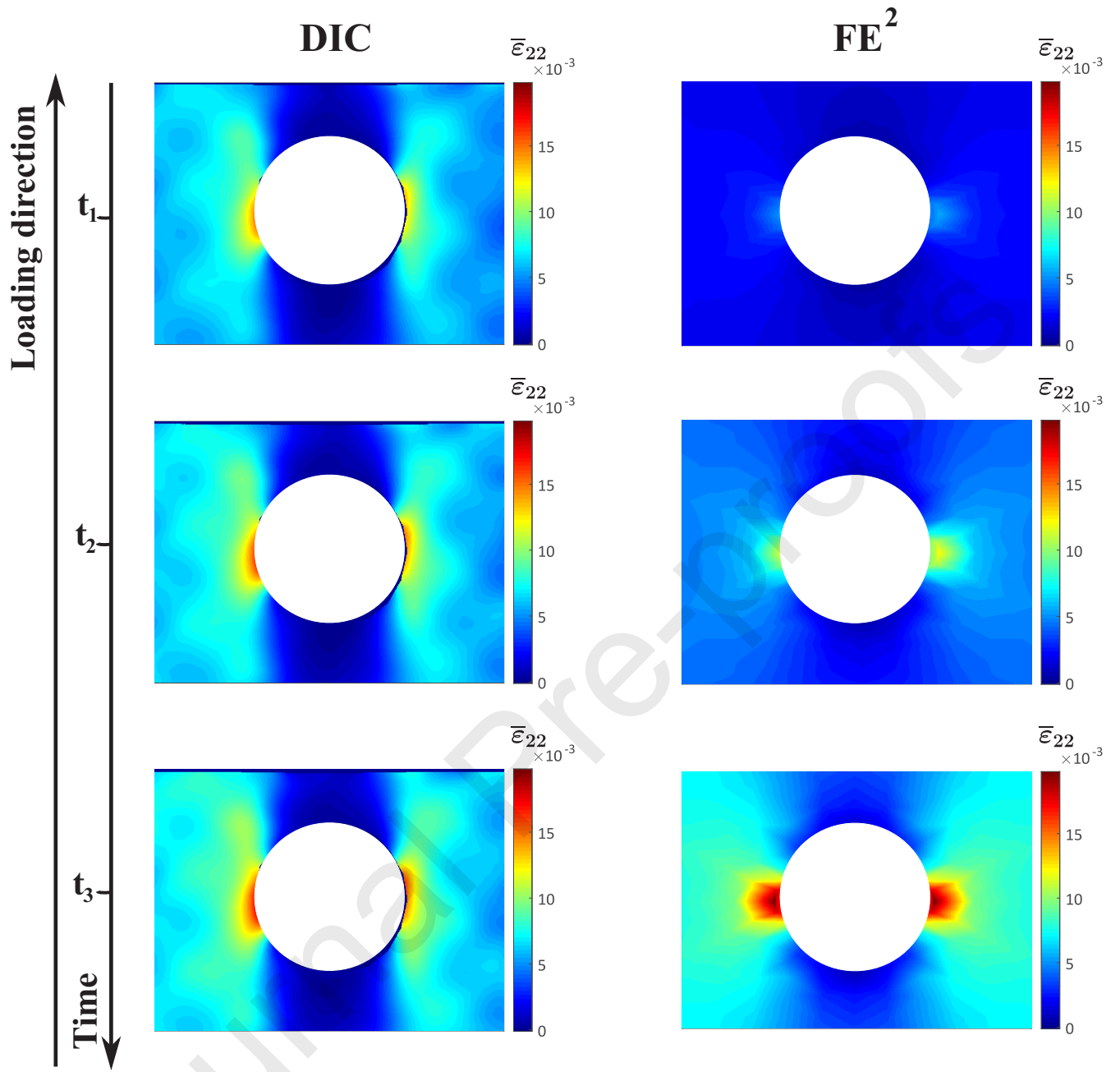


Figure 15: Longitudinal strain fields of the  $\pm 90$  composite assessed at  $t_1$ ,  $t_2$  and  $t_3$  showing both DIC and FE<sup>2</sup> results for  $\dot{u}_y = 0.24 \text{ mm.s}^{-1}$ .

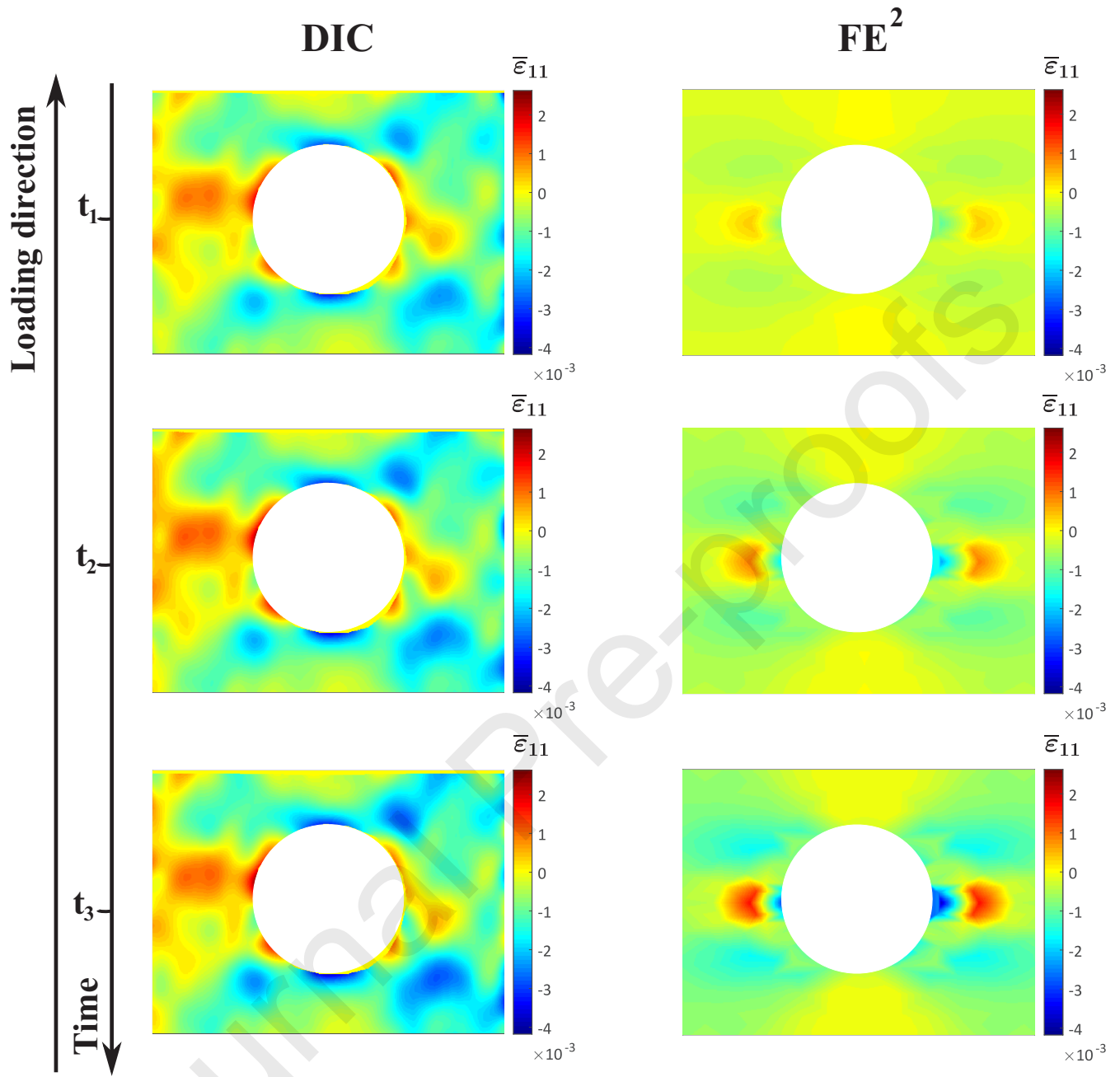


Figure 16: Transverse strain fields of the  $\pm 90^\circ$  composite assessed at  $t_1$ ,  $t_2$  and  $t_3$  showing both DIC and FE<sup>2</sup> results for  $\dot{u}_y = 0.24 \text{ mm.s}^{-1}$ .

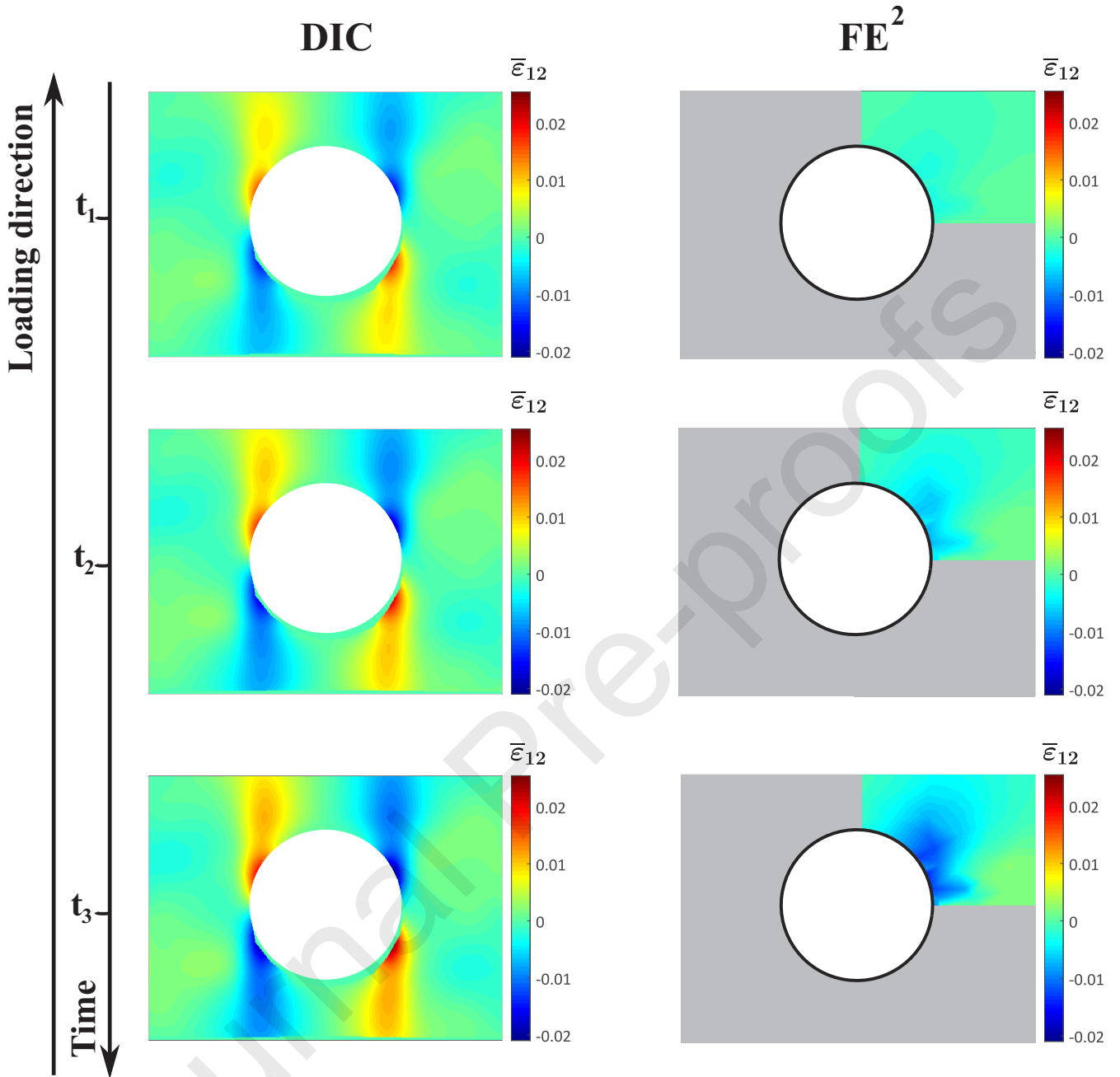


Figure 17: Shear strain fields of the  $\pm 90$  composite assessed at  $t_1$ ,  $t_2$  and  $t_3$  showing both DIC and  $FE^2$  results for  $\dot{u}_y = 0.24 \text{ mm.s}^{-1}$ .

### 5.2.2. $\pm 45$ woven composite

Fig. 18 presents both DIC and  $FE^2$  longitudinal strain fields,  $\bar{\epsilon}_{22}$ , for the  $\pm 45$  composite at the three selected times  $t_1$ ,  $t_2$  and  $t_3$ . Figs. 19 and 20 present the transverse,  $\bar{\epsilon}_{11}$ , and shear,  $\bar{\epsilon}_{12}$ , strain components at  $t_3$  for both DIC and  $FE^2$  under the loading rate of  $0.33 \text{ mm.s}^{-1}$ .

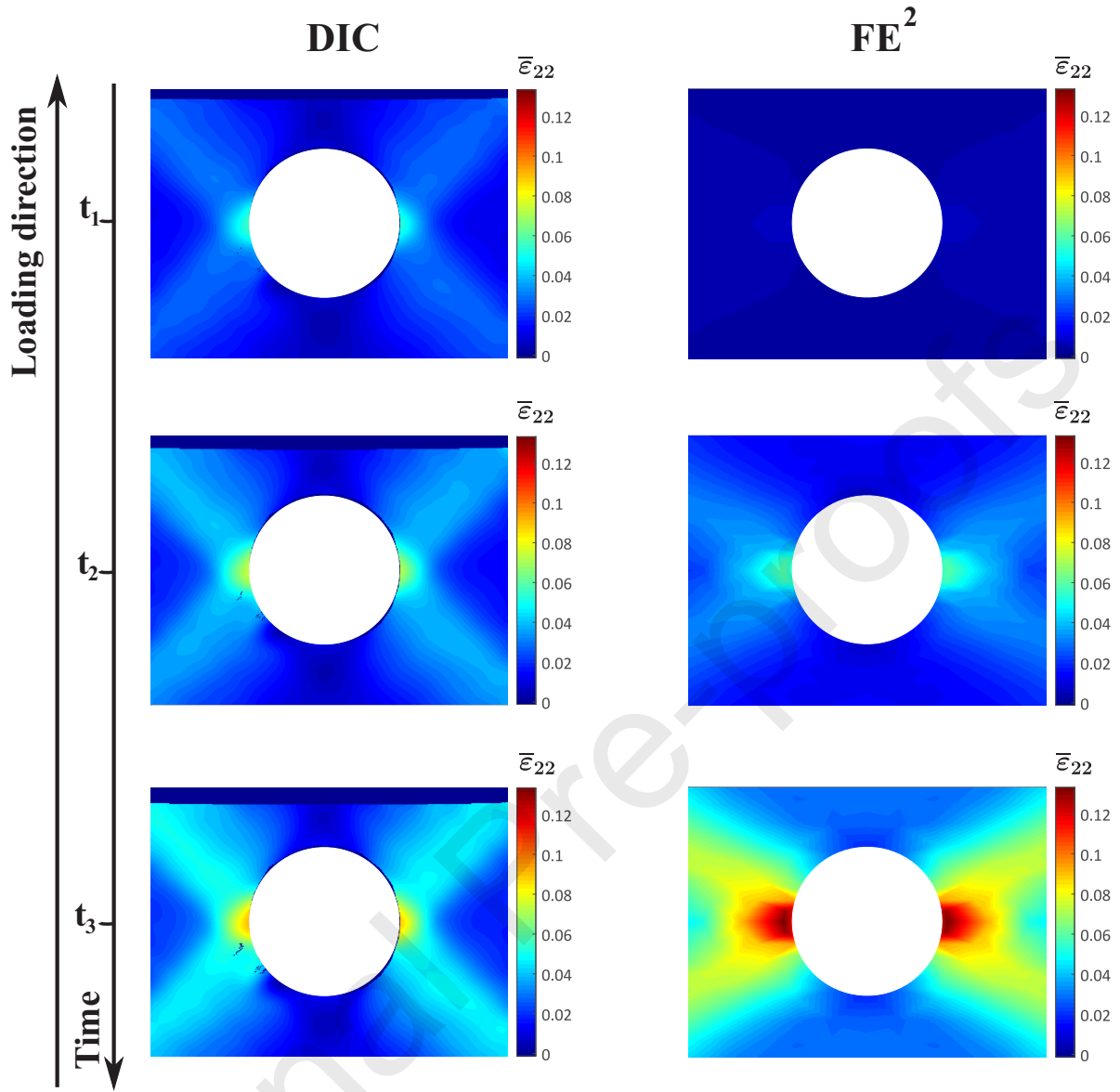


Figure 18: Longitudinal strain fields of the  $\pm 45$  composite assessed at  $t_1$ ,  $t_2$  and  $t_3$  showing both DIC and  $FE^2$  results for  $\dot{u}_y = 0.33 \text{ mm.s}^{-1}$ .

It can be seen from Fig. 18 that the  $FE^2$  results are close to those of the DIC approach with hotspots well captured by the multi-scale model. However, clear differences in the spatio-temporal distribution and the order of magnitude are observed for both transverse and shear strain components (Figs. 19 and 20). These differences can be explained by: i) the macroscopic boundary conditions applied to the structure as well as the assumed symmetry conditions on the FE model of the macro-structure, ii) the periodicity condition of the microstructure that is not “scrupulously” taken into account in the width direction of the perforate plate, iii) the non-inclusion of damage mechanisms in the yarns, such as decohesion in the yarns/matrix



interface, inter-yarns friction and yarns rotation when the composite is loaded in its shear plane.

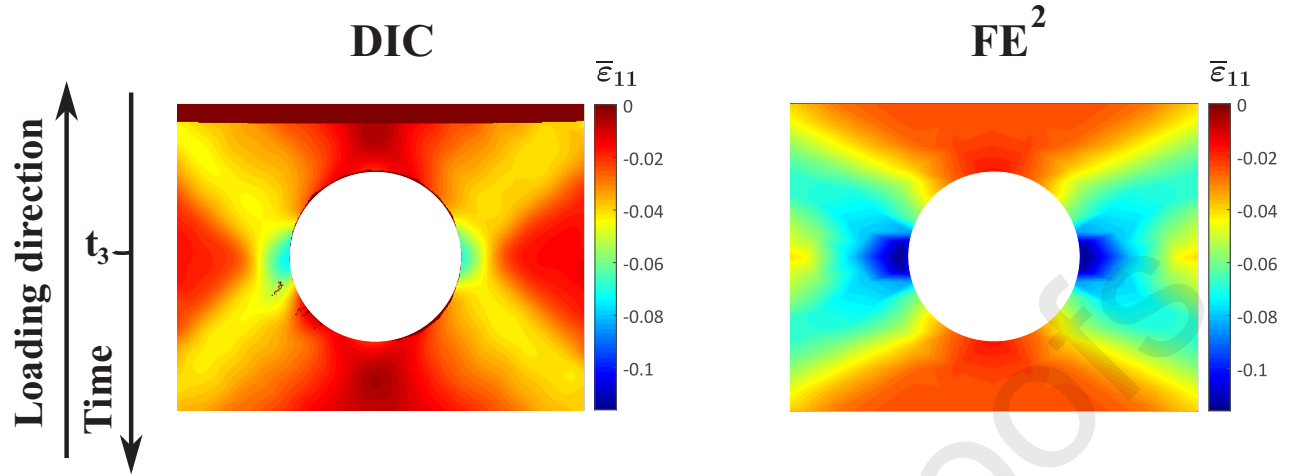


Figure 19: Transverse strain fields of the  $\pm 45^\circ$  composite assessed at  $t_3$  showing both DIC and FE<sup>2</sup> results for  $\dot{u}_y = 0.33 \text{ mm.s}^{-1}$ .

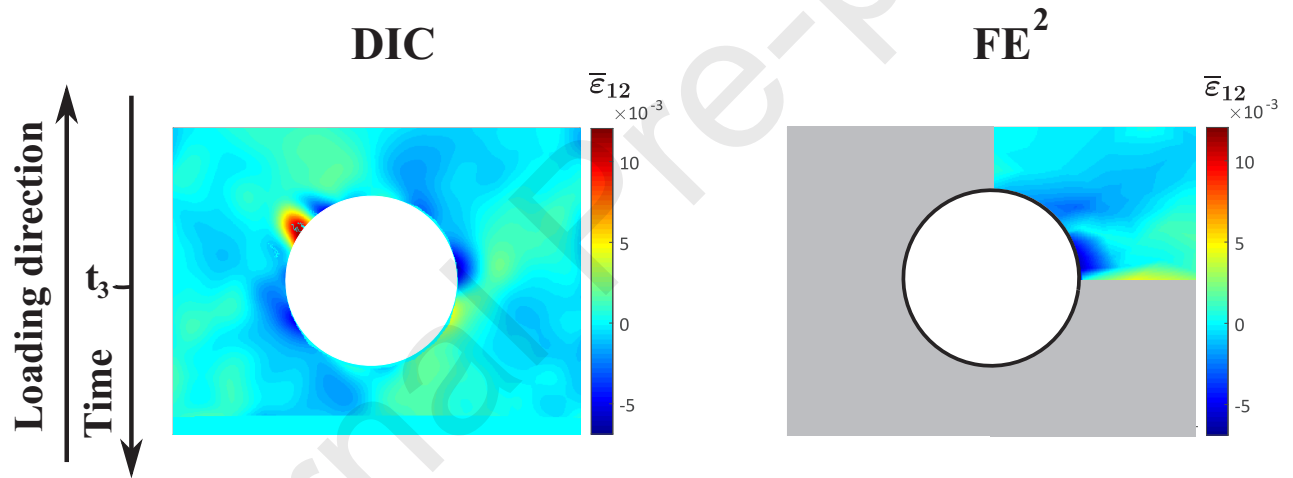


Figure 20: Shear strain fields of the  $\pm 45^\circ$  composite assessed at  $t_3$  showing both DIC and FE<sup>2</sup> results for  $\dot{u}_y = 0.33 \text{ mm.s}^{-1}$ .

### 5.2.3. $\pm 30^\circ$ woven composite

Fig. 21 presents a comparison of the spatio-temporal distribution of both DIC and FE<sup>2</sup> longitudinal strain components results captured at  $t_1$ ,  $t_2$  and  $t_3$  for a loading rate  $0.33 \text{ mm.s}^{-1}$ . Figs. 22 and 23 present the spatial distribution of the transverse and shear components at  $t_3$ . For the longitudinal strain component, the multi-scale approach results are quite similar to those of the experimental approach (Fig. 21). However, a significant difference is observed for the normal transverse and shear components (Fig. 22 and Fig. 23). The reasons for these discrepancies

are the same as those reported in the previous subsection. Indeed, off-axis loading causes significant rotations between the yarns in the microstructure, which in turn causes decohesion in the yarns/matrix interfaces. These aspects are not taken into account in the numerical approach.

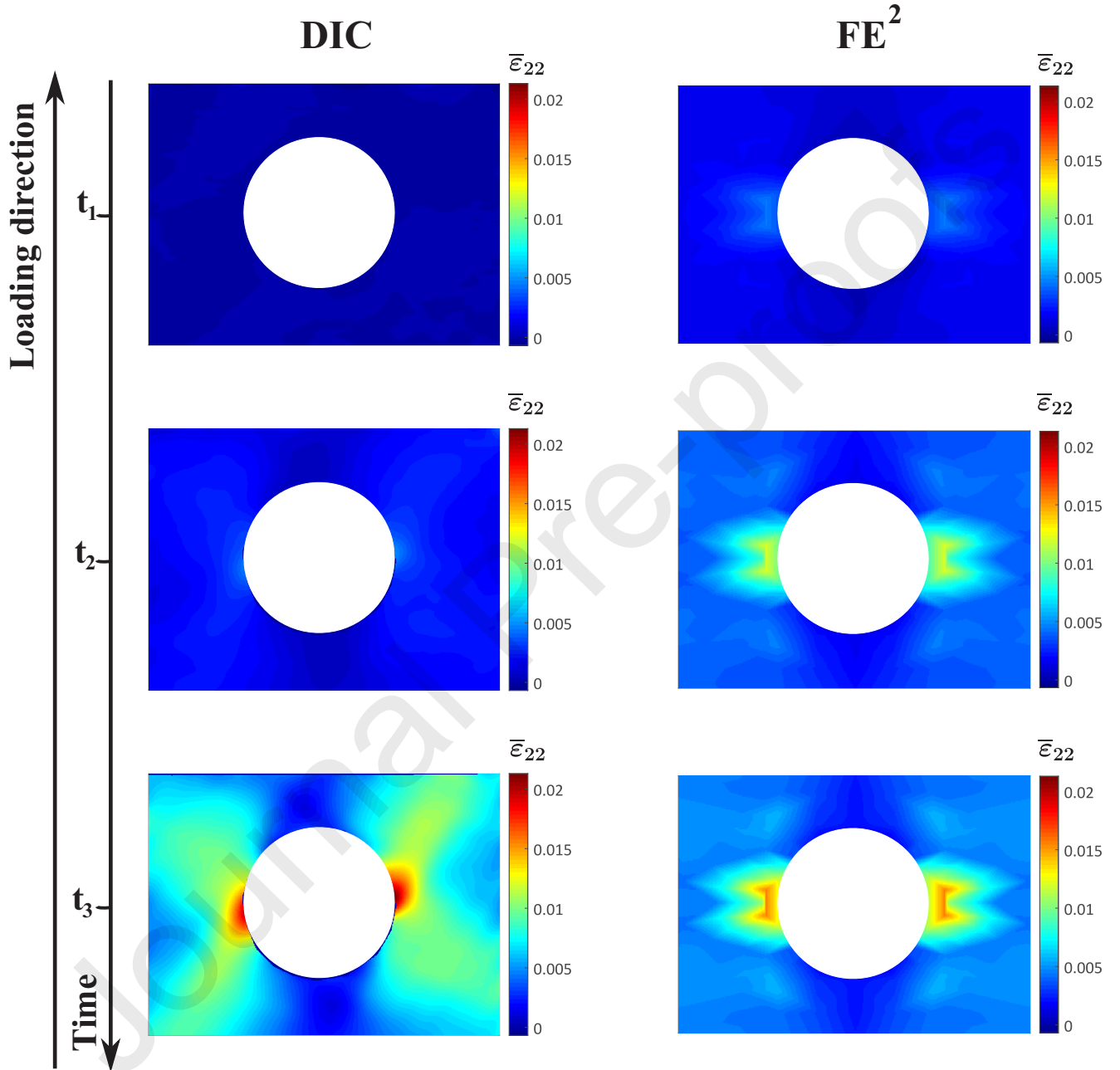


Figure 21: Longitudinal strain fields of the  $\pm 30$  composite assessed at  $t_1$ ,  $t_2$  and  $t_3$  showing both DIC and  $\text{FE}^2$  results for  $\dot{u}_y = 0.33 \text{ mm.s}^{-1}$ .

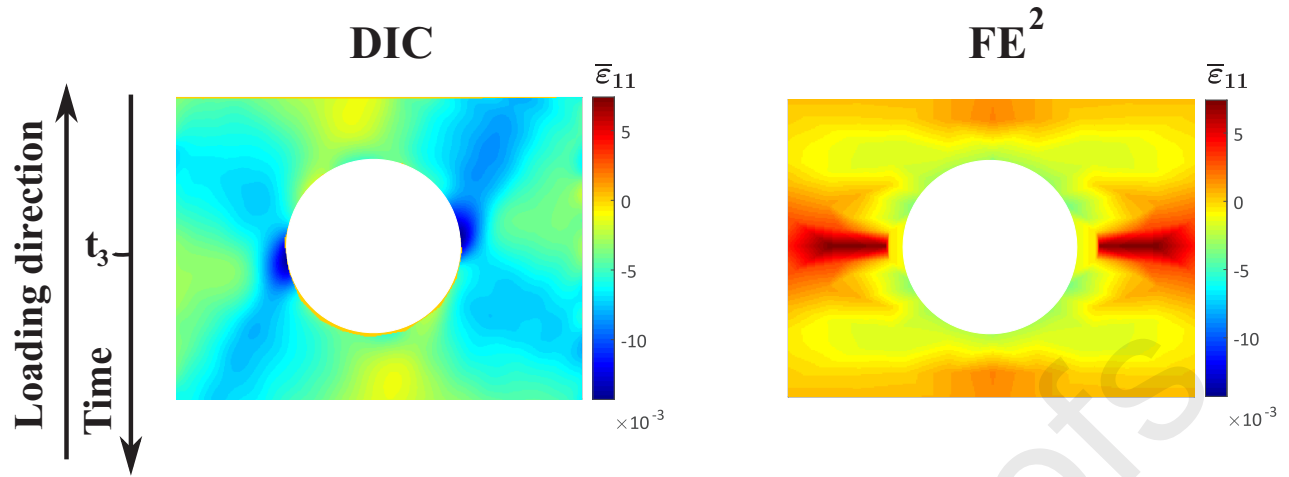


Figure 22: Transverse strain fields of the  $\pm 30$  composite assessed at  $t_3$  showing both DIC and FE<sup>2</sup> results for  $\dot{u}_y = 0.33 \text{ mm.s}^{-1}$ .

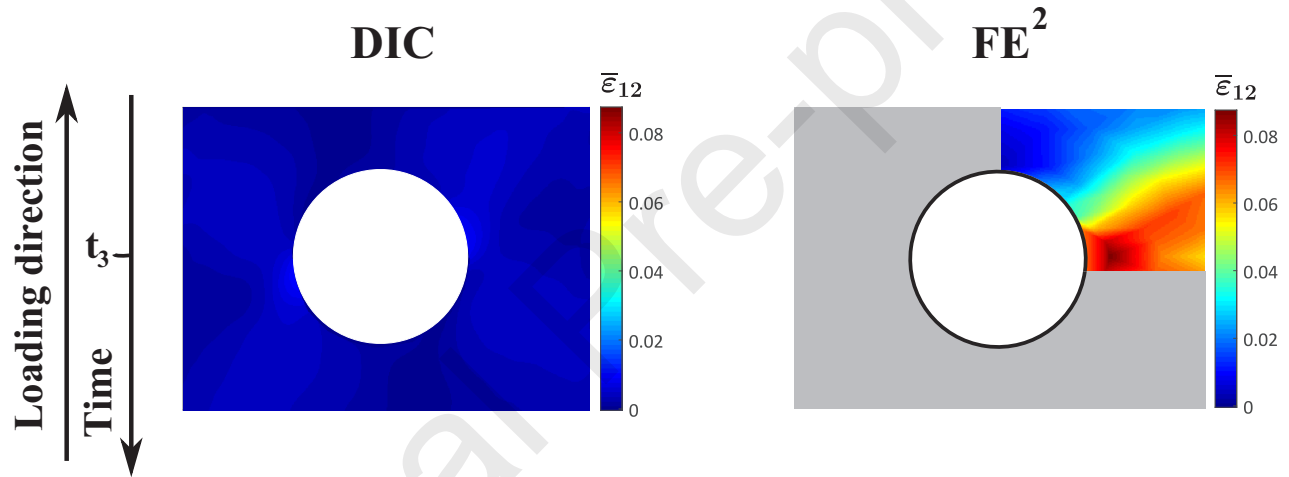


Figure 23: Shear strain fields of the  $\pm 30$  composite assessed at  $t_3$  showing both DIC and FE<sup>2</sup> results for  $\dot{u}_y = 0.33 \text{ mm.s}^{-1}$ .

Overall, the developed FE<sup>2</sup> strategy gives quite reliable predictions on different stacking sequence configurations. These results are very satisfactory for such complex structural analysis. Nevertheless, the integration of other complex mechanisms in the constitutive laws (rotation of the yarns, interfacial damage, etc.) is important for capturing more accurately the structure's response during the off-axes loading.

## 6. Macro-micro analysis of the mechanical response of the woven composite

In this section, the capacities of the FE<sup>2</sup> approach to describe and capture the mechanical response and the dissipative behaviour of the studied composite at different scales are discussed.

To do so, the macroscopic and microscopic numerical results extracted from the monotonic tensile tests are presented and investigated for both  $\pm 90$  and  $\pm 30$  composite configurations.

### 6.1. $FE^2$ approach for the $\pm 90$ composite

#### 6.1.1. Macroscopic fields

Fig. 24 presents the spatial distribution of the macroscopic stress fields computed using the  $FE^2$  approach, as well as the microscopic stress distribution at unit cells of selected macroscopic points. It can be seen that the maximum longitudinal stress is located at the frontiers of the hole (point A as indicated in Fig. 24-b). On the other hand, the most stressed point on compression in direction 1 is in point B (Fig. 24-a). The latter finding is also observed experimentally.

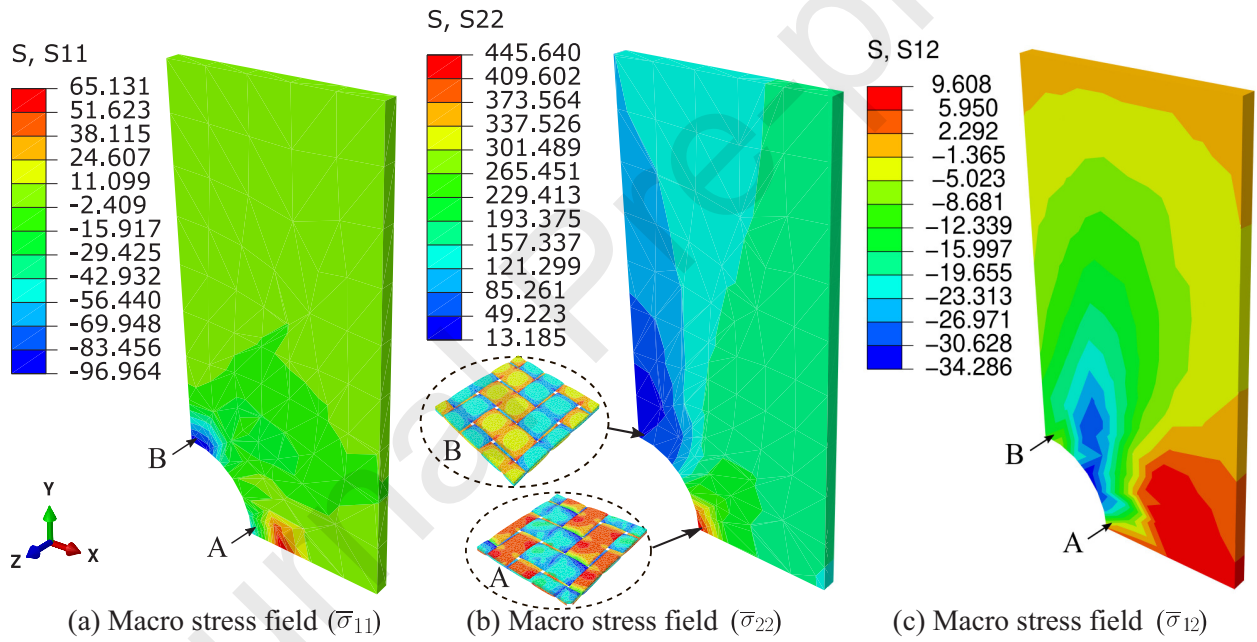


Figure 24: Spatial distribution of the macroscopic stress fields ( $\bar{\sigma}_{11}$ ,  $\bar{\sigma}_{22}$  and  $\bar{\sigma}_{12}$ ) in the perforated plate computed through the  $FE^2$  approach for the  $\pm 90$  configuration.

Fig. 25 illustrates the macroscopic stress-strain curves at the point A of the longitudinal, transverse and shear strain components for the strain rates  $0.24$  and  $0.024 \text{ mm.s}^{-1}$ . The maximum stress is observed in the loading direction,  $\bar{\sigma}_{22}$ . Fig. 26 illustrates the stress-strain curves at the point B for the same loading rates. These figures clearly show that the most important stress is in the compression direction,  $\bar{\sigma}_{11}$ . The out of plane stress  $\sigma_{33}$  is very small for both rates. This is expected due to the low thickness of the composite holed plate.

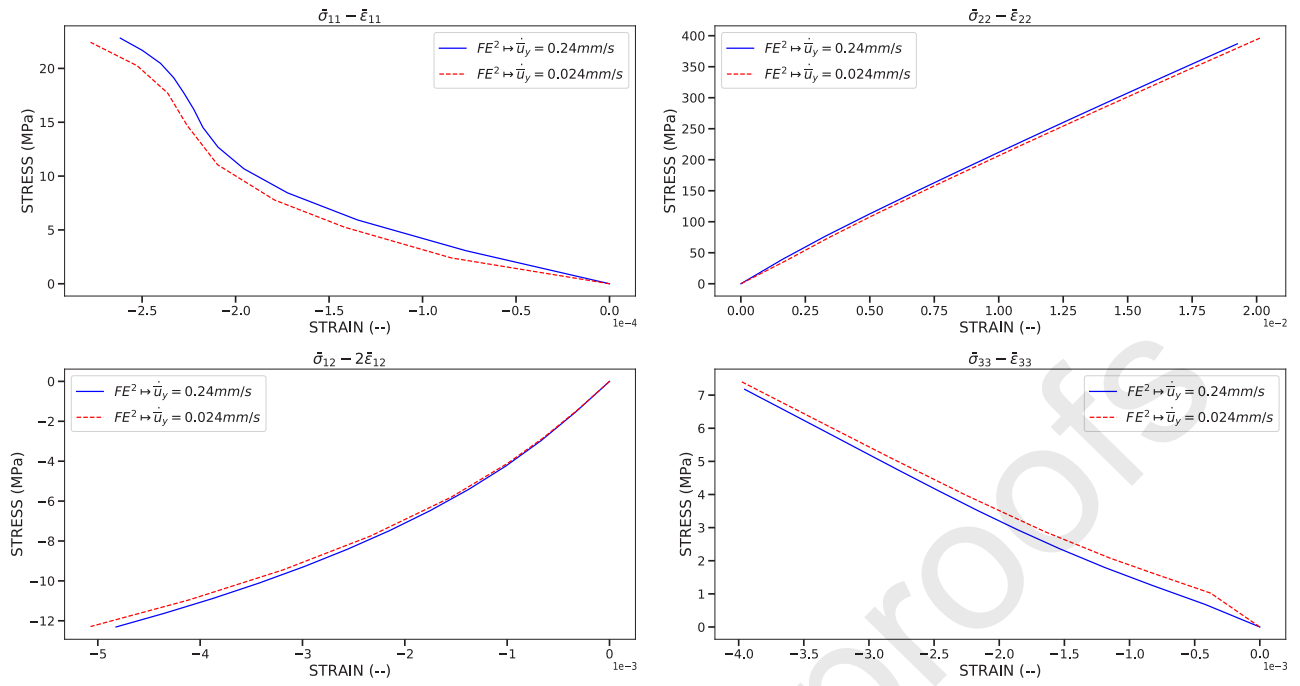


Figure 25: Macroscopic mechanical responses of the  $\pm 90$  composite configuration at point A of the structure computed using the  $FE^2$  approach for the components 11, 22, 33 and 12 under both loading rates 0.24 and 0.024  $\text{mm.s}^{-1}$ .

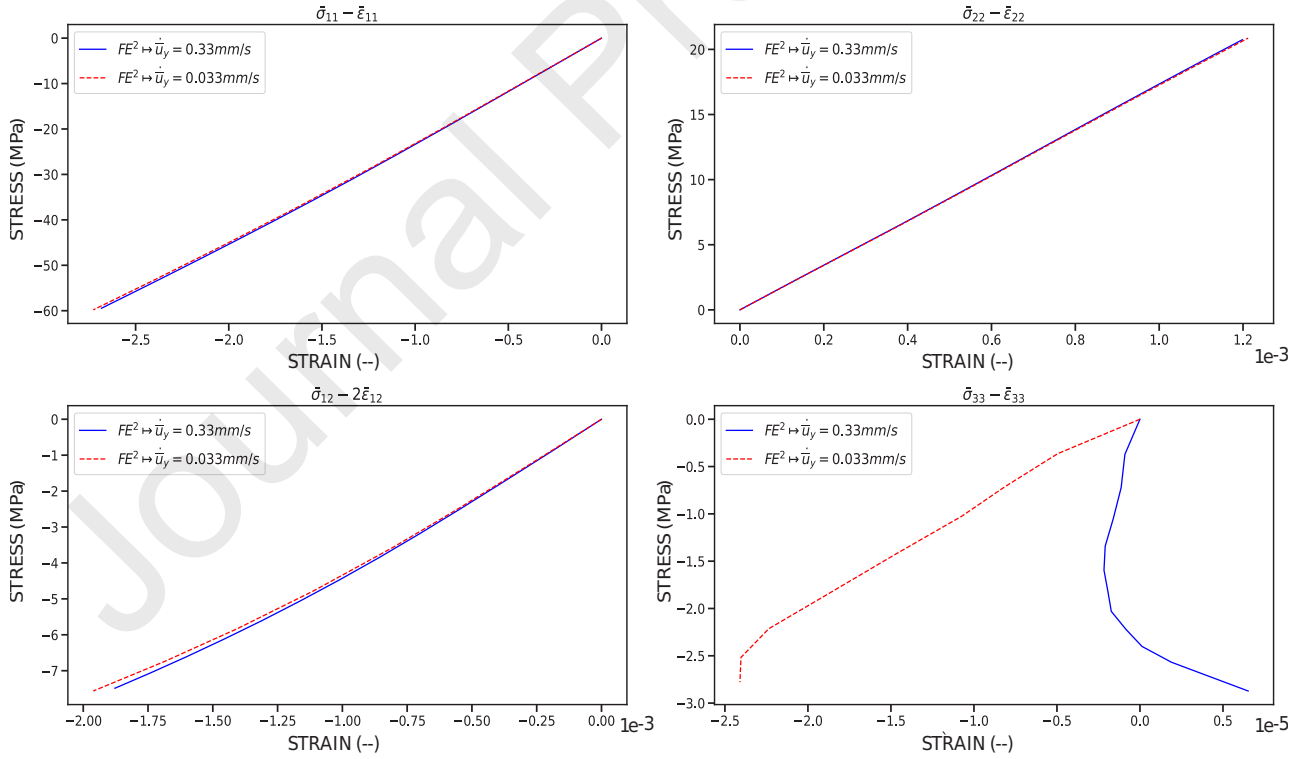


Figure 26: Macroscopic mechanical responses of the  $\pm 90$  composite configuration at point B of the structure computed using the  $FE^2$  approach for the components 11, 22, 33 and 12 under both loading rates 0.24 and 0.024  $\text{mm.s}^{-1}$ .

### 6.1.2. Microscopic fields

Figs. 27 and 28 present the local stress fields in the microstructure at points A and B of the macro-structure during the last stages of the loading. Fig. 27-b demonstrates that, when the composite is mainly loaded in the weft direction, most of the load is carried by the weft yarns in their transverse direction. Meanwhile, a small part of this load is also carried by the warp yarns in their longitudinal direction (Fig. 27-d). This causes micro-cracks concentration in the yarns-crossing areas, as can be seen in Fig. 27-h. The same observation holds for the in-plane shear 12 component (Fig. 27-f). For the matrix, most of the stress concentration is observed in the yarns-crossing areas, as can be seen in Figs. 27-a, -c and -e. This may lead to softening within the matrix and/or fracture in the yarns. Such aspect is not taken into account in the proposed constitutive models used in the  $FE^2$  approach. In addition, it is worth noting that extremely high stress magnitudes in some specific zones of yarns-crossing are indeed computational artifact and cannot be avoided since the proposed constitutive models do not account for fracture or localization effects.



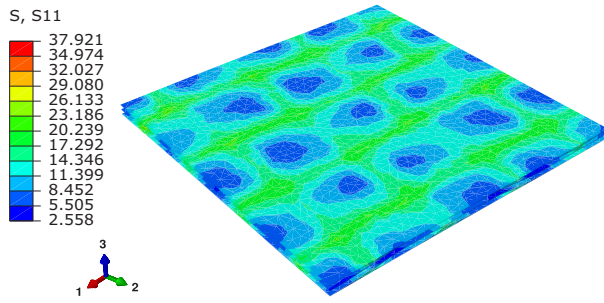
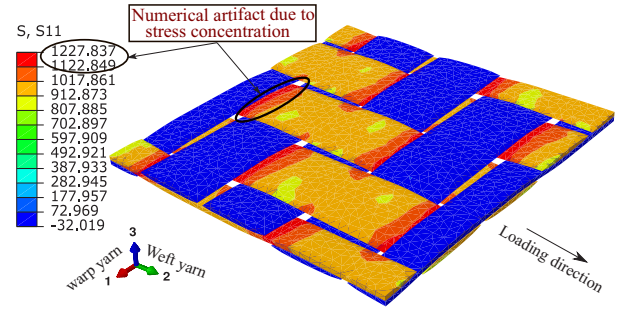
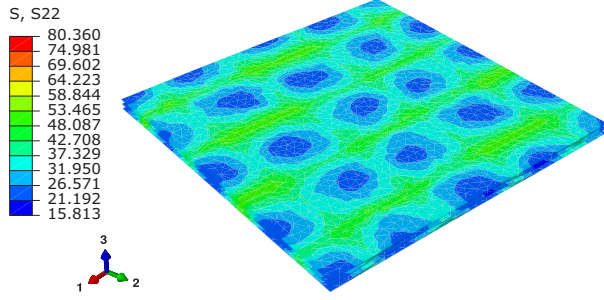
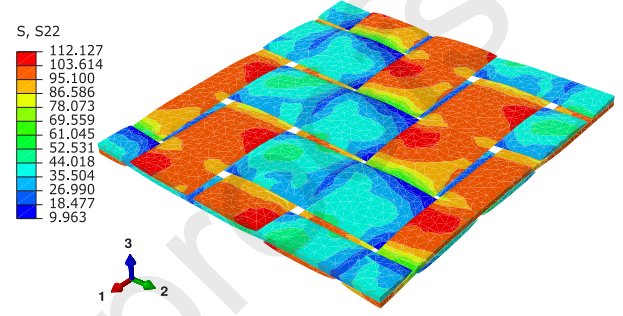
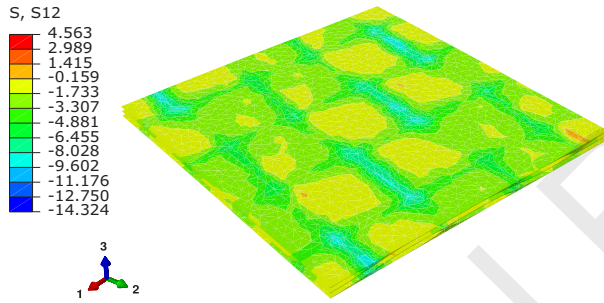
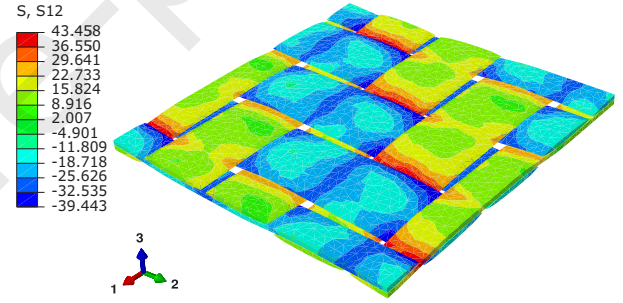
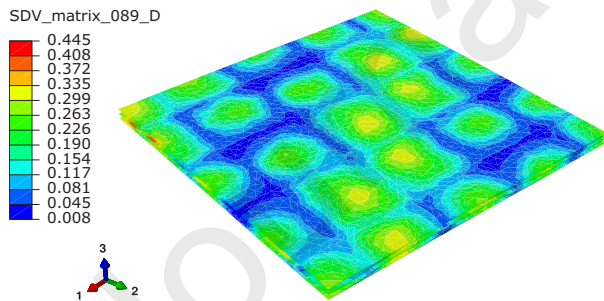
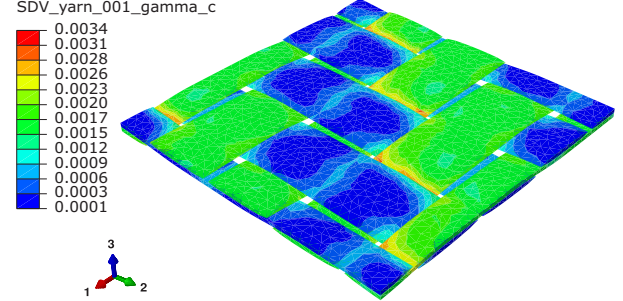
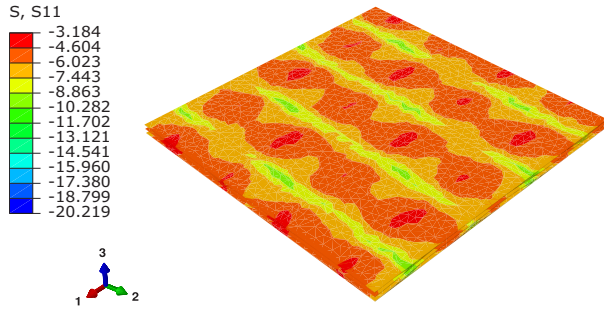
(a) Local longitudinal stress,  $\sigma_{11}$ , in the matrix.(b) Local longitudinal stress,  $\sigma_{11}$ , in the yarns.(c) Local transverse stress,  $\sigma_{22}$ , in the matrix.(d) Local transverse stress,  $\sigma_{22}$ , in the yarns.(e) Local in-plane shear stress,  $\sigma_{12}$ , in the matrix.(f) Local in-plane shear stress ( $\sigma_{12}$ ) in the yarns(g) Local damage ( $D$ ) in the matrix.(h) Local micro-crack density ( $\gamma_c$ ) in the yarns.

Figure 27: Local stress fields at the point A of the  $\pm 90$  composite structure assessed at the end of the  $0.24 \text{ mm.s}^{-1}$  monotonic tensile test. Note that the local stresses in the yarns are expressed in the local coordinate system of each yarn material point.

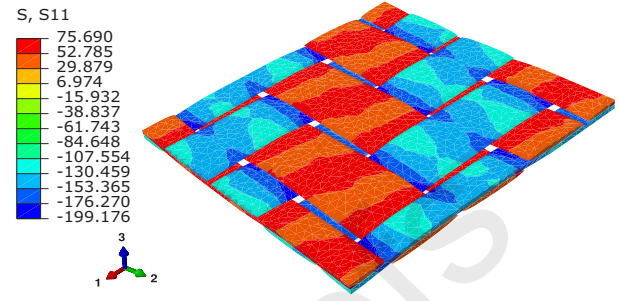
Fig. 28 illustrates that most of the compression load induced by the Poisson effect is driven by the warp yarns in their longitudinal direction (Fig. 28-b). Moreover, an amount of this load is supported by the weft yarns (Fig. 28-d), causing slight micro-cracking in the crossing directions



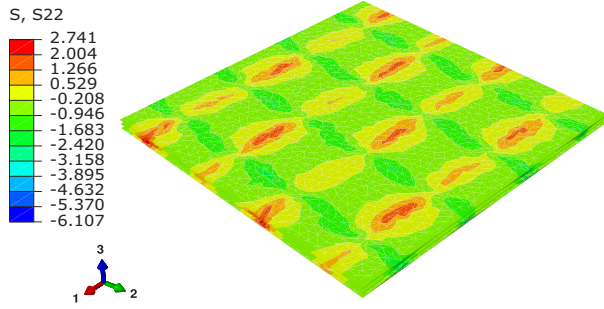
of the yarns (Fig. 28-h). Figs. 28-a, -c and -e confirm that most of the stress at point B is transferred to the yarns. Therefore, there is no damage in the matrix at this point, as indicated in Fig. 28-g.



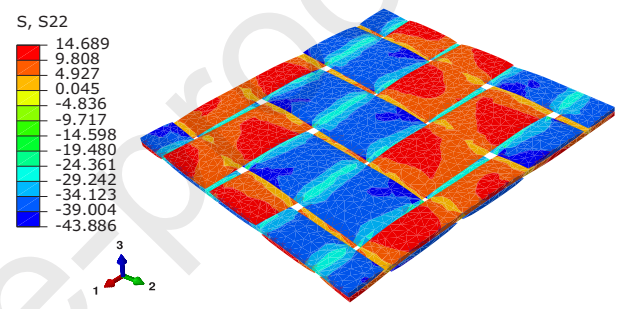
(a) Local longitudinal stress,  $\sigma_{11}$ , in the matrix.



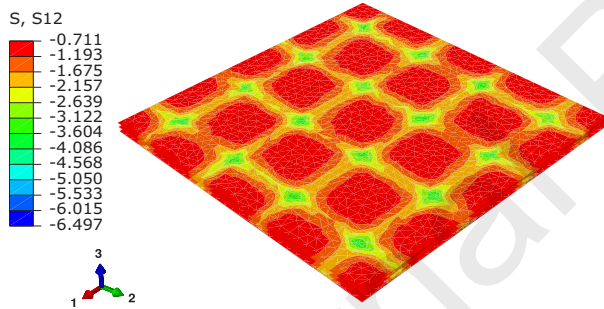
(b) Local longitudinal stress,  $\sigma_{11}$ , in the yarns.



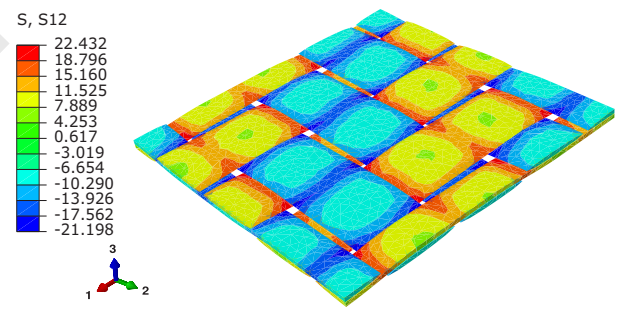
(c) Local transverse stress,  $\sigma_{22}$ , in the matrix.



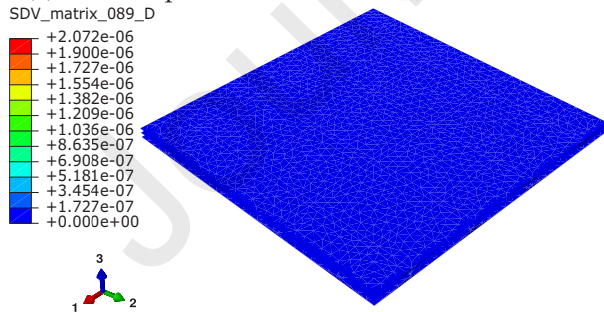
(d) Local transverse stress,  $\sigma_{22}$ , in the yarns.



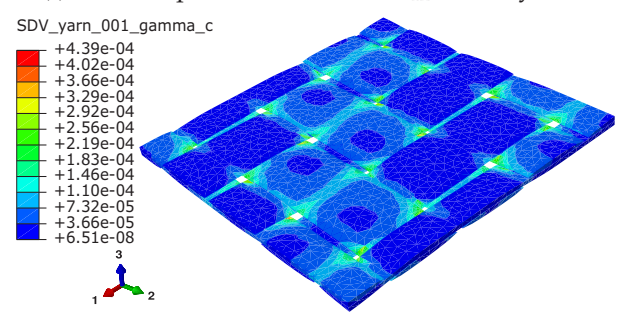
(e) Local in-plane shear stress,  $\sigma_{12}$ , in the matrix.



(f) Local in-plane shear stress,  $\sigma_{12}$ , in the yarns.



(g) Local damage,  $D$ , in the matrix.



(h) Local micro-crack density,  $\gamma_c$ , in the yarns.

Figure 28: Local stress fields at the point A of the  $\pm 90$  composite structure assessed at the end of the  $0.24 \text{ mm.s}^{-1}$  monotonic tensile test.

## 6.2. $FE^2$ approach for the $\pm 30$ composite

### 6.2.1. Macroscopic fields

Figure 29 illustrates the spatial distribution of the macroscopic normal stresses in the directions 1 and 2 and the macroscopic shear stress 12. Fig. 30 presents the stress-strain curves at the point A of the components  $\bar{\sigma}_{11}$ ,  $\bar{\sigma}_{22}$ ,  $\bar{\sigma}_{33}$  and  $\bar{\sigma}_{12}$  for both loading rates 0.033 and 0.33 mm.s<sup>-1</sup>. A quasi-linear mechanical response with negligible rate effect is observed in the direction of the warp and weft yarns. On the other hand, a significant non-linearity appears in the shear response with a rate effect becoming more important, as demonstrated in Fig. 30. This result is due to the off-axis loading conditions of the composite, which involves a significant non-linearity in the shear direction caused by the rheology of the matrix, its damage and the micro-cracks in the yarns.

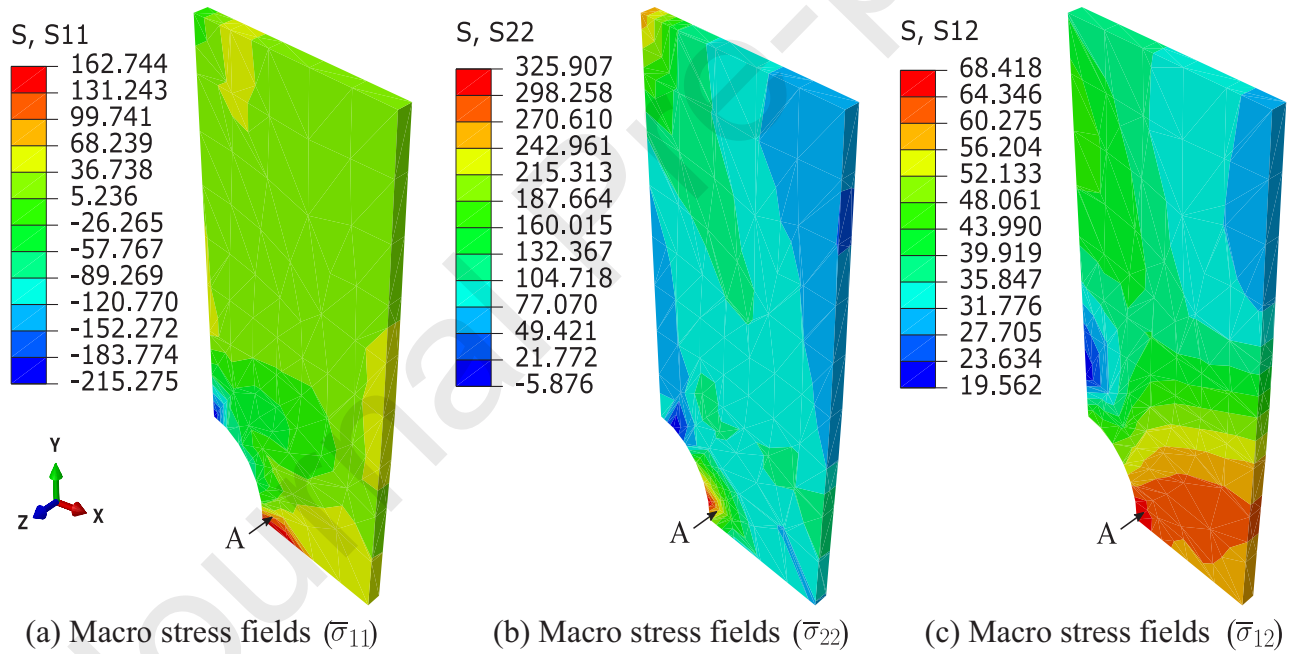


Figure 29: Macroscopic stress fields distribution associated with the components  $\bar{\sigma}_{11}$ ,  $\bar{\sigma}_{22}$  and  $\bar{\sigma}_{12}$  in the macro-structure for the  $\pm 30$  configuration, estimated through the proposed  $FE^2$  approach.

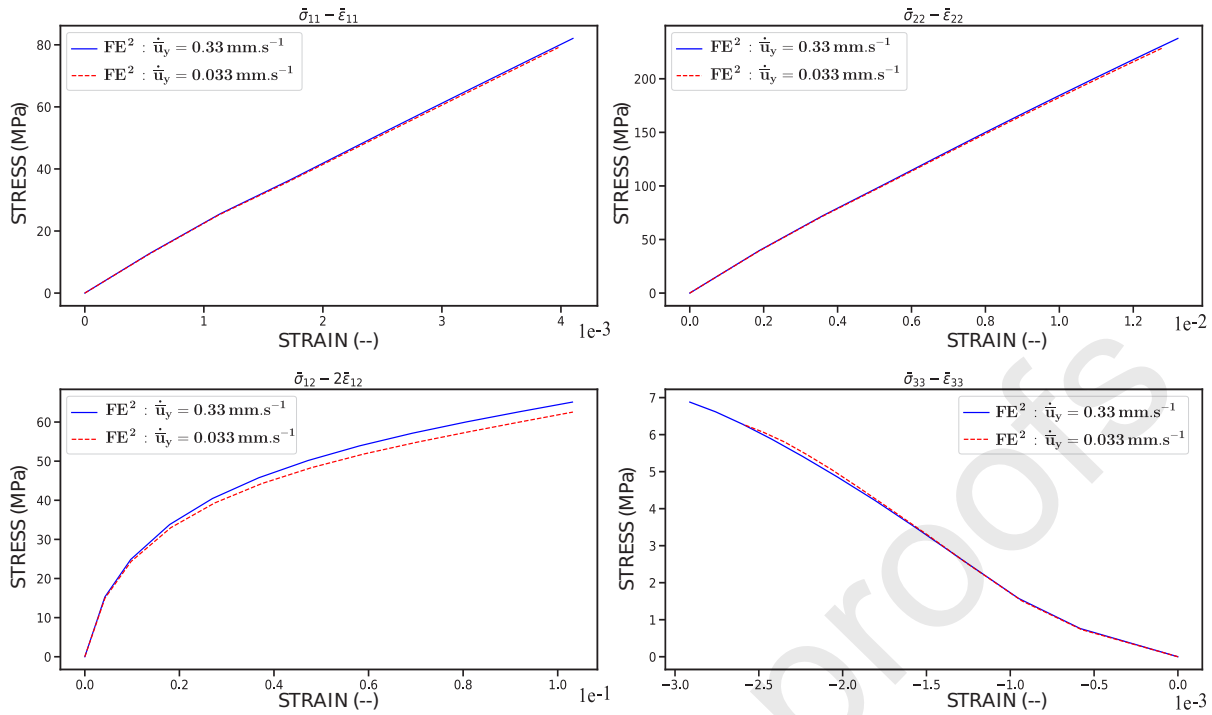


Figure 30: Macroscopic mechanical responses of the  $\pm 30$  composite configuration at the point A of the structure estimated through the FE<sup>2</sup> approach for the components 11, 22, 33 and 12. The loading rates were set at 0.033 and 0.33 mm.s<sup>-1</sup>.

### 6.2.2. Microscopic fields

Fig. 31 shows the microscopic stress fields distribution in the matrix and in the yarns, while Fig. 32 illustrates the progressive spatio-temporal evolution of the damage within the two phases, as well as the micro-cracks density evolution in the yarns.

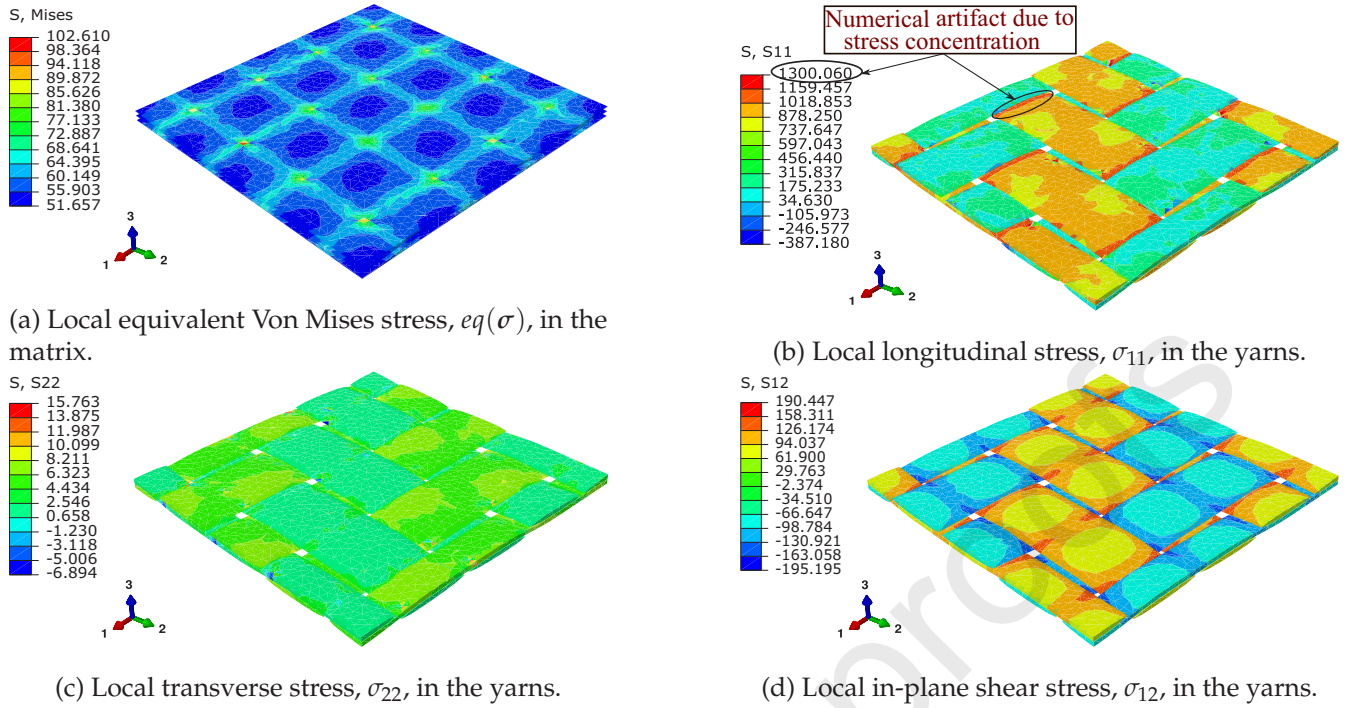
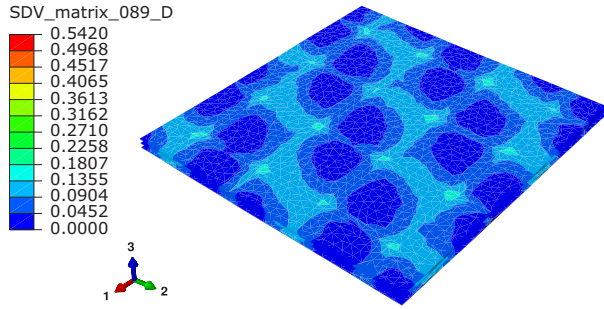


Figure 31: Local stress fields at the point A of the  $\pm 30$  composite structure assessed at the end of the  $0.33 \text{ mm.s}^{-1}$  monotonic tensile test.

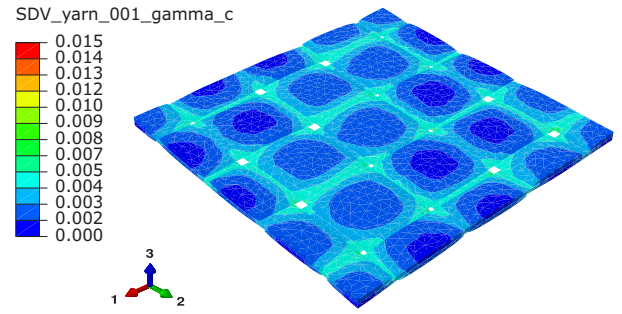
It can be seen that the microstructure undergoes both tensile stress in the weft yarns direction and compression in the warp yarns direction (Fig. 31-b). The microstructure is also subjected to 12 shear stress (Fig. 31-d), where the local stresses in the warp and weft yarns are reversed. This causes stress concentrations in the crossing zones of the yarns which can lead to a fast micro-cracks evolution in the warp and weft yarns (Fig. 32-f). In addition, the overall load is progressively transferred to the matrix where the stresses are mainly concentrated in the inter-yarns areas (Fig. 31-a) and the damage within the matrix develops progressively, as shown in Fig. 32-e. These damage mechanisms have a significant effect on the macroscopic response of the composite especially in the 12 shear behaviour.

The progressive spatio-temporal evolution of the damage within the matrix (Fig. 32) is mainly located in the yarns-crossing areas. It can be seen from the figure that the degradation is developed progressively within the warp, weft yarns direction and essentially between the yarns. Indeed, when the matrix is locally damaged, a part of the load is progressively transferred to the yarns. This is due to the microstructure interactions which are accompanied by an increase in the intra-yarns micro-cracks density.

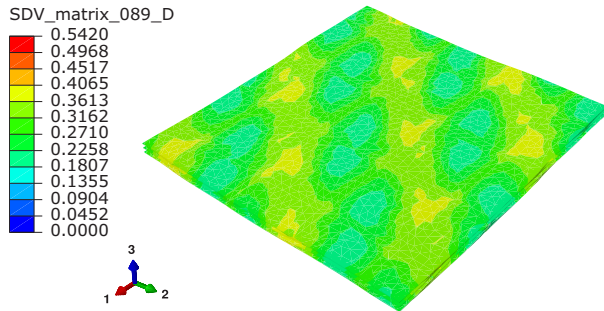




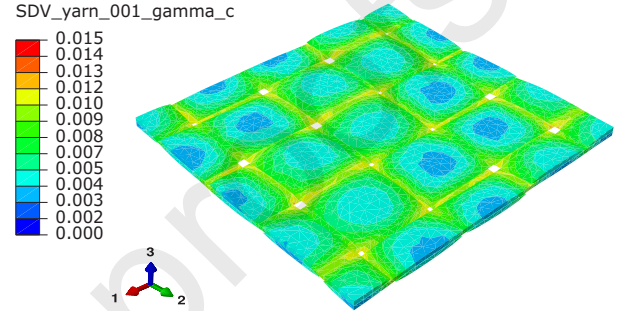
(a) Local damage,  $D$ , in the matrix at ( $t = 1.8$  s).



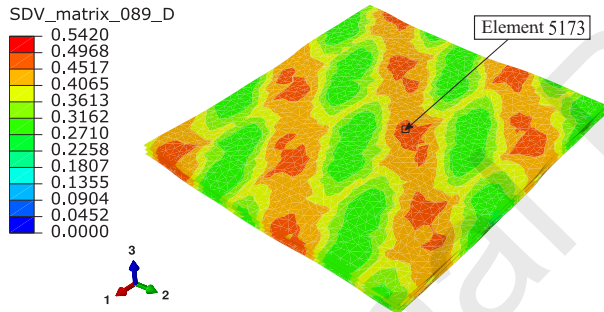
(b) Local micro-crack density,  $\gamma_c$ , in the yarns at ( $t = 1.8$  s).



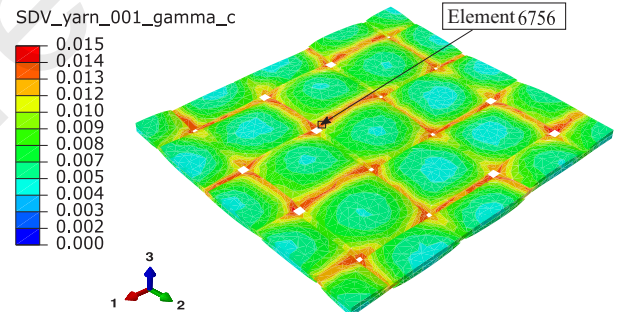
(c) Local damage,  $D$ , in the matrix at ( $t = 3.4$  s).



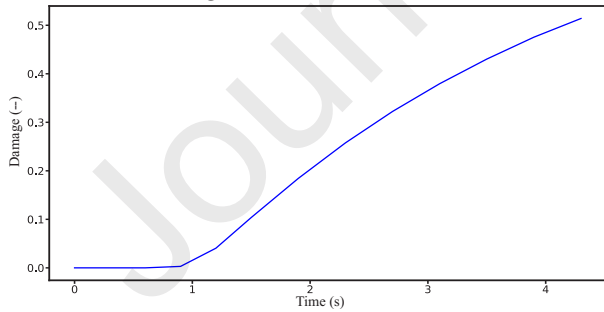
(d) Local micro-crack density,  $\gamma_c$ , in the yarns at ( $t = 3.4$  s).



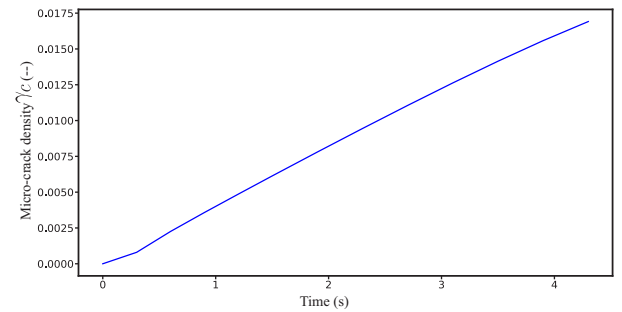
(e) Local damage,  $D$ , in the matrix at ( $t = 4.2$  s).



(f) Local micro-crack density,  $\gamma_c$ , in the yarns at ( $t = 4.2$  s).



(g) Local damage,  $D$ , evolution in the yarns for the element 5173 marked above in Fig. 32-e.



(h) Local micro-crack density,  $\gamma_c$ , evolution in the yarns for the element 6756 marked above in Fig. 32-f.

Figure 32: Spatio-temporal evolution of the damage,  $D$ , in the matrix and the micro-cracks density,  $\gamma_c$ , in the yarns at the three selected analysis times:  $t = 1.8$  s,  $t = 3.4$  s and  $t = 4.2$  s for the  $\pm 30$  composite configuration.

## 7. Conclusions and further work

This work presents an experimental validation of the multi-scale three-dimensional modeling strategy for thermoplastic-based woven composites structures, using the  $FE^2$  framework developed in [Tikarrouchine et al. \(2018\)](#). The approach is fully integrated in the finite element commercial code Abaqus/Standard, using parallel computations. The main advantage of the approach is their modularity and capacity to integrate any type of composites with periodic microstructure.

The numerical results obtained by the  $FE^2$  calculation on a perforated plate are compared with the experimental results for three stacking sequences configurations ( $[0^0]$ ,  $[\pm 30^0]$  and  $[\pm 45^0]$ ). Strongly nonlinear local constitutive models integrating the rheology (VE-VP) in the PA66 matrix and its ductile damage as well as the degradation in the yarns (transverse damage) are used and assembled through the multi-scale  $FE^2$  approach, to predict the macroscopic behavior of the studied composite, taking into account the effects of the microstructure observed in each constituent of the unit cell.

The periodic unit cell that represents the microstructure at each macroscopic integration point of the studied composite was generated using microstructural data obtained by X-ray microtomography. The parameters of the two behavior models were identified in the work of [Praud \(2018\)](#) at RH50 % for the thermoplastic matrix as well as for the yarns. The performances and the capacities of the proposed approach were highlighted through comparisons between the numerical predictions and the experimental results obtained for three configurations of stacking sequence.

The experimental results obtained by DIC show an acceptably good agreement with the numerical simulations using ( $FE^2$  calculation). Indeed, despite the challenge to capture the microstructural effects through multiscale FE computations, the obtained results exhibit a relative quantitative and qualitative consistency in the trends. These results highlight the performances and the capabilities of the proposed approach to predict the spatio-temporal evolution of the various phenomena observed on the microstructure level, namely rheology and the damage initiation and propagation in the matrix as well as micro-cracks accumulation in the yarns,

etc. The results also show the ability of the approach to capture the anisotropic response of the composite material induced by the microstructure effects, time dependency and the strain rate effects of the thermoplastic matrix. In a future work, the use of infrared thermography for the full-field temperature measurement will be combined with the DIC technique towards the experimental validation of the computationally efficient multiscale (FE<sup>2</sup>) method that has been already extended to the fully coupled thermomechanical framework [Tikarrouchine et al. \(2019\)](#); [Berthelsen and Menzel \(2019\)](#). Besides the kinematic fields, the combination will allow capturing the local thermomechanical responses as well as the coupling of the damage with the local dissipations and its influence on the temperature variations during a thermomechanical loading. **Moreover, further investigations on the sensitivity analysis for material parameters and geometric uncertainties can be considered in order to improve the accuracy of the approach** [Naouar et al. \(2014\)](#); [Green et al. \(2014\)](#); [Huang et al. \(2020a,b\)](#).

## References

- Allaire, G., 1992. Homogenization and two-scale convergence. *SIAM Journal on Mathematical Analysis* 23, 1482–1518.
- Angioni, S.L., Meo, M., Foreman, A., 2011. A comparison of homogenization methods for 2-D woven composites. *Composites Part B* 42, 181–189.
- Anzelotti, G., Nicoletto, G., Riva, E., 2008. Mesomechanic strain analysis of twill-weave composite lamina under unidirectional in-plane tension. *Composites Part A: Applied Science and Manufacturing* 39, 1294–1301.
- Arif, M., Meraghni, F., Chemisky, Y., Despringre, N., Robert, G., 2014. In situ damage mechanisms investigation of PA66/GF30 composite: Effect of relative humidity. *Composites Part B: Engineering* 58, 487–495.
- Arruda, E.M., Boyce, M.C., Jayachandran, R., 1995. Effects of strain rate, temperature and thermomechanical coupling on the finite strain deformation of glassy polymers. *Mechanics of Materials* 19, 193–212.



- Asada, T., Ohno, N., 2007. Fully implicit formulation of elastoplastic homogenization problem for two-scale analysis. *International Journal of Solids and Structures* 44, 7261 – 7275.
- Bednarczyk, B.A., Stier, B., Simon, J.W., Reese, S., Pineda, E.J., 2015. Meso- and micro-scale modeling of damage in plain weave composites. *Composite Structures* 121, 258–270.
- Behera, B., Dash, B., 2015. Mechanical behavior of 3d woven composites. *Materials and Design* 67, 261 – 271.
- Bensoussan, A., Lions, J., Papanicolaou, G., 1978. Asymptotic methods for periodic structures. North Holland, Amsterdam.
- Berthelsen, R., Denzer, R., Oppermann, P., Menzel, A., 2017. Computational homogenisation for thermoviscoplasticity: application to thermally sprayed coatings. *Computational Mechanics* 60, 739–766.
- Berthelsen, R., Menzel, A., 2019. Computational homogenisation of thermo-viscoplastic composites: Large strain formulation and weak micro-periodicity. *Computer Methods in Applied Mechanics and Engineering* 348, 575 – 603.
- Boubakar, M.L., Trivaudey, F., Perreux, D., Vang, L., 2002. A meso-macro finite element modelling of laminate structures - Part I : Time-independent behaviour. *Journal of Composite Structures* 58, 271–286.
- Boufaïda, Z., 2015. Analyse des propriétés mécaniques de composites taffetas verre/matrice acrylique en relation avec les propriétés d'adhésion des fibres sur la matrice. Ph.D. thesis. Université de lorraine -Institut National Polytechnique de Lorraine.
- Carvelli, V., Poggi, C., 2001. A homogenization procedure for the numerical analysis of woven fabric composites. *Composites Part A: Applied Science and Manufacturing* 32, 1425–1432.
- Charalambakis, N., Chatzigeorgiou, G., Chemisky, Y., Meraghni, F., 2018. Mathematical homogenization of inelastic dissipative materials: a survey and recent progress. *Continuum Mechanics and Thermodynamics* 30, 1–51.

- Chatzigeorgiou, G., Charalambakis, N., Chemisky, Y., Meraghni, F., 2016. Periodic homogenization for fully coupled thermomechanical modeling of dissipative generalized standard materials. *International Journal of Plasticity* 81, 18–39.
- Chatzigeorgiou, G., Charalambakis, N., Chemisky, Y., Meraghni, F., 2018. *Thermomechanical Behavior of Dissipative Composite Materials*. ISTE Press - Elsevier, London.
- Chatzigeorgiou, G., Chemisky, Y., Meraghni, F., 2015. Computational micro to macro transitions for shape memory alloy composites using periodic homogenization. *Smart Materials and Structures* 24, 035009.
- Chemisky, Y., Meraghni, F., Bourgeois, N., Cornell, S., Echchorfi, R., Patoor, E., 2015. Analysis of the deformation paths and thermomechanical parameter identification of a shape memory alloy using digital image correlation over heterogeneous tests. *International Journal of Mechanical Sciences* 96-97, 13–24.
- Dai, S., Cunningham, P., Marshall, S., Silva, C., 2015. Influence of fibre architecture on the tensile, compressive and flexural behaviour of 3d woven composites. *Composites Part A: Applied Science and Manufacturing* 69, 195 – 207.
- Detrez, F., Cantournet, S., Seguela, R., 2011. Plasticity/damage coupling in semi-crystalline polymers prior to yielding: Micromechanisms and damage law identification. *Polymer* 52, 1998–2008.
- Feyel, F., 1999. Multiscale FE2 elastoviscoplastic analysis of composite structures. *Computational Materials Science* 16, 344–354.
- Feyel, F., Chaboche, J.L., 2000. Fe2 multiscale approach for modelling the elastoviscoplastic behaviour of long fibre sic/ti composite materials. *Computer Methods in Applied Mechanics and Engineering* 183, 309 – 330.
- Germain, P., 1973. *Cours de mécanique des milieux continus, Tome I: Théorie Générale*. Masson, Paris.

- Germain, P., 1982. Sur certaines définitions liées à l'énergie en mécanique des solides. *International Journal of Engineering Science* 20, 245–259.
- Green, S., Matveev, M., Long, A., Ivanov, D., Hallett, S., 2014. Mechanical modelling of 3d woven composites considering realistic unit cell geometry. *Composite Structures* 118, 284 – 293.
- Grmela, M., Lebon, G., 1990. Hamiltonian extended thermodynamics. *Journal of Physics A: Mathematical and General* 23, 3341–3351.
- Guillaume, C., 2008. Multiscale modeling of the mechanical behavior of woven composite materials. Ph.D. thesis. Université Sciences et Technologies - Bordeaux I.
- He, C., Ge, J., Zhang, B., Gao, J., Zhong, S., Liu, W.K., Fang, D., 2020. A hierarchical multiscale model for the elastic-plastic damage behavior of 3d braided composites at high temperature. *Composites Science and Technology* , 108230.
- Hochard, C., Aubourg, P.A., Charles, J.P., 2001. Modelling of the mechanical behaviour of woven-fabric CFRP laminates up to failure. *Composites Science and Technology* 61, 221–230.
- Hochard, C., Payan, J., Bordreuil, C., 2006. A progressive first ply failure model for woven ply CFRP laminates under static and fatigue loads. *International Journal of Fatigue* 28, 1270–1276.
- Hochard, C., Thollon, Y., 2010. A generalized damage model for woven ply laminates under static and fatigue loading conditions. *International Journal of Fatigue* 32, 158–165.
- Huang, W., Causse, P., Hu, H., Belouettar, S., Trochu, F., 2020a. Transverse compaction of 2d glass woven fabrics based on material twins – part i: Geometric analysis. *Composite Structures* 237, 111929.
- Huang, W., Causse, P., Hu, H., Belouettar, S., Trochu, F., 2020b. Transverse compaction of 2d glass woven fabrics based on material twins – part ii: Tow and fabric deformations. *Composite Structures* 237, 111963.
- Javili, A., Chatzigeorgiou, G., Steinmann, P., 2013. Computational homogenization in magneto-mechanics. *International Journal of Solids and Structures* 50, 4197–4216.

- Jou, D., Casas-Vázquez, J., Lebon, G., 1999. Extended irreversible thermodynamics revisited (1988-98). *Reports on Progress in Physics* 62, 1035–1142.
- Krasnobrizha, A., 2015. Modelling of the hysteretic behavior of woven composite using a collaborative elastoplastic damaged model with fractional derivatives . Ph.D. thesis. Ecole Centrale Nantes, Université Bretagne Loire ; Institut de Recherche en Génie Civil et Mécanique – UMR CNRS 6183.
- Krasnobrizha, A., Rozycki, P., Cosson, P., Gornet, L., 2016. Modélisation des mécanismes d’hystérésis des composites tissés à l’aide d’un modèle collaboratif élasto-plastique endommageable à dérivées fractionnaires. *Matériaux & Techniques* 104, 407.
- Ladeveze, P., LeDantec, E., 1992. Damage modelling of the elementary ply for laminated composites. *Composites Science and Technology* 43, 257–267.
- Launay, A., Marco, Y., Maitournam, M.H., Raoult, I., 2013. Modelling the influence of temperature and relative humidity on the time-dependent mechanical behaviour of a short glass fibre reinforced polyamide. *Mechanics of Materials* 56, 1–10.
- Lemaitre, J., 1985. Coupled elasto-plasticity and damage constitutive equations. *Computer Methods in Applied Mechanics and Engineering* 51, 31–49.
- Lemaitre, J., Chaboche, J.L., 1990. *Mechanics of solid materials*. Cambridge University Press.
- Lemaitre, J., Desmorat, R., 2005. *Engineering damage mechanics : ductile, creep, fatigue and brittle failure*. Springer.
- Lin, H., Brown, L.P., Long, A.C., 2011. Modelling and simulating textile structures using texgen, in: *Advances in Textile Engineering*, Trans Tech Publications. pp. 44–47.
- Mahboob, Z., Chemisky, Y., Meraghni, F., Bougherara, H., 2017. Mesoscale modelling of tensile response and damage evolution in natural fibre reinforced laminates. *Composites Part B: Engineering* 119, 168–183.

- Malpot, A., Touchard, F., Bergamo, S., 2015. Effect of relative humidity on mechanical properties of a woven thermoplastic composite for automotive application. *Polymer Testing* 48, 160–168.
- Margueres, P., Meraghni, F., 2013. Damage induced anisotropy and stiffness reduction evaluation in composite materials using ultrasonic wave transmission. *Composites Part A: Applied Science and Manufacturing* 45, 134–144.
- Meraghni, F., Nouri, H., Bourgeois, N., Czarnota, C., Lory, P., 2011. Parameters identification of fatigue damage model for short glass fiber reinforced polyamide (PA6-GF30) using digital image correlation. *Procedia Engineering* 10, 2110–2116.
- Mori, T., Tanaka, K., 1973. Average stress in matrix and average elastic energy of materials with misfitting inclusions. *Acta Metallurgica* 21, 571–574.
- Murat, F., Tartar, L., 1997. H-convergence, in *Topics in the mathematical modelling of composite materials*, in: Cherkaev, A., Kohn, R.V. (Eds.), *Progress in Nonlinear Differential Equations and their Applications*. Birkhäuser, Boston. volume 31, pp. 21–43.
- Naouar, N., Vidal-Sallé, E., Schneider, J., Maire, E., Boisse, P., 2014. Meso-scale fe analyses of textile composite reinforcement deformation based on x-ray computed tomography. *Composite Structures* 116, 165 – 176.
- Nezamabadi, S., Yvonnet, J., Zahrouni, H., Potier-Ferry, M., 2009. A multilevel computational strategy for handling microscopic and macroscopic instabilities. *Computer Methods in Applied Mechanics and Engineering* 198, 2099 – 2110.
- Nezamabadi, S., Zahrouni, H., Yvonnet, J., Potier-Ferry, M., 2010. A multiscale finite element approach for buckling analysis of elastoplastic long fiber composites. *International Journal for Multiscale Computational Engineering* 8, 287–301.
- Nouri, H., 2008. Modélisation et identification de lois de comportement avec endommagement en fatigue polycyclique de matériaux composites à matrice thermoplastique. Ph.D. thesis. ENSAM. Paris.

- Nouri, H., Meraghni, F., Lory, P., 2009. Fatigue damage model for injection-molded short glass fibre reinforced thermoplastics. *International Journal of Fatigue* 31, 934–942.
- Papadopoulos, V., Tavlaki, M., 2016. The impact of interfacial properties on the macroscopic performance of carbon nanotube composites. a fe2-based multiscale study. *Composite Structures* 136, 582 – 592.
- Pomarède, P., Meraghni, F., Peltier, L., Delalande, S., Declercq, N.F., 2018. Damage Evaluation in Woven Glass Reinforced Polyamide 6.6/6 Composites Using Ultrasound Phase-Shift Analysis and X-ray Tomography. *Journal of Nondestructive Evaluation* 37, 12.
- Praud, F., 2018. Multi-scale modelling of thermoplastic-based woven composites, cyclic and time-dependent behaviour. Ph.D. thesis. Ecole Nationale Supérieure d'Arts et Métiers - ENSAM.
- Praud, F., Chatzigeorgiou, G., Bikard, J., Meraghni, F., 2017a. Phenomenological multi-mechanisms constitutive modelling for thermoplastic polymers, implicit implementation and experimental validation. *Mechanics of Materials* 114, 9–29.
- Praud, F., Chatzigeorgiou, G., Chemisky, Y., Meraghni, F., 2017b. Hybrid micromechanical-phenomenological modelling of anisotropic damage and anelasticity induced by micro-cracks in unidirectional composites. *Composite Structures* 182, 223–236.
- Puck, A., Schürmann, H., 2002. Failure analysis of FRP laminates by means of physically based phenomenological models. *Composites Science and Technology* 62, 1633–1662.
- Qi, M., Giraud, A., Colliat, J., Shao, J., 2016. A numerical damage model for initially anisotropic materials. *International Journal of Solids and Structures* 100-101, 245–256.
- Rique, O., Liu, X., Yu, W., Byron Pipes, R., 2020. Constitutive modeling for time- and temperature-dependent behavior of composites. *Composites Part B: Engineering* 184, 107726.
- Rouf, K., Liu, X., Yu, W., 2018. Multiscale structural analysis of textile composites using mechanics of structure genome. *International Journal of Solids and Structures* 136-137, 89 – 102.

- Ruijter, W., 2009. Analysis of mechanical properties of woven textile composites as a function of textile geometry. Ph.D. thesis. University of Nottingham.
- Saleh, M.N., Lubineau, G., Potluri, P., Withers, P.J., Soutis, C., 2016. Micro-mechanics based damage mechanics for 3d orthogonal woven composites: Experiment and numerical modelling. *Composite Structures* 156, 115–124.
- Sanchez-Palencia, E., 1978. Non-homogeneous media and vibration theory, in: *Lecture Notes in Physics* 127. Springer-Verlag, Berlin.
- Schröder, J., Labusch, M., Keip, M.A., 2016. Algorithmic two-scale transition for magneto-electro-mechanically coupled problems: Fe2-scheme: Localization and homogenization. *Computer Methods in Applied Mechanics and Engineering* 302, 253 – 280.
- Scida, D., Aboura, Z., Benzeggagh, M., Bocherens, E., 1999. A micromechanics model for 3d elasticity and failure of woven-fibre composite materials. *Composites Science and Technology* 59, 505–517.
- Sengupta, A., Papadopoulos, P., Taylor, R.L., 2012. A multiscale finite element method for modeling fully coupled thermomechanical problems in solids. *International Journal for Numerical Methods in Engineering* 91, 1386–1405.
- Sherburn, M., 2007. Geometric and mechanical modelling of textiles. Ph.D. thesis. University of Nottingham.
- Soden, J., Weissenbach, G., Hill, B., 1999. The design and fabrication of 3d multi-layer woven t-section reinforcements. *Composites Part A: Applied Science and Manufacturing* 30, 213 – 220.
- Suquet, P.M., 1987. Elements of homogenization for inelastic solid mechanics, in: *Lecture Notes in Physics*. Springer, Berlin. volume 272, pp. 193–278.
- Tabiei, A., Yi, W., 2002. Comparative study of predictive methods for woven fabric composite elastic properties. *Composite Structures* 58, 149–164.



- Tan, V.B.C., Raju, K., Lee, H.P., 2020. Direct fe2 for concurrent multilevel modelling of heterogeneous structures. *Computer Methods in Applied Mechanics and Engineering* 360, 112694.
- Tang, X., Whitcomb, J.D., 2003. Progressive Failure Behaviors of 2D Woven Composites. *Journal of Composite Materials* 37, 1239–1259.
- Tchalla, A., Belouettar, S., Makradi, A., Zahrouni, H., 2013. An abaqus toolbox for multiscale finite element computation. *Composites Part B: Engineering* 52, 323 – 333.
- Terada, K., Kikuchi, N., 2001. A class of general algorithms for multi-scale analyses of heterogeneous media. *Computer Methods in Applied Mechanics and Engineering* 190, 5427–5464.
- Tikarrouchine, E., Chatzigeorgiou, G., Chemisky, Y., Meraghni, F., 2019. Fully coupled thermoviscoplastic analysis of composite structures by means of multi-scale three-dimensional finite element computations. *International Journal of Solids and Structures* 164, 120–140.
- Tikarrouchine, E., Chatzigeorgiou, G., Praud, F., Piotrowski, P., Chemisky, Y., Meraghni, F., 2018. Three-dimensional fe2 method for the simulation of non-linear, rate-dependent response of composite structures. *Composite Structures* 193, 165–179.
- Wang, L., Wu, J., Chen, C., Zheng, C., Li, B., Joshi, S.C., Zhou, K., 2017. Progressive failure analysis of 2d woven composites at the meso-micro scale. *Composite Structures* 178, 395–405.
- Xu, R., Yang, J., Yan, W., Huang, Q., Giunta, G., Belouettar, S., Zahrouni, H., Ben Zineb, T., Hu, H., 2020. Data-driven multiscale finite element method: From concurrence to separation. *Computer Methods in Applied Mechanics and Engineering* 363, 112893.
- Zhou, L., Chen, M.W., Liu, C., Wu, H., 2018. A multi-scale stochastic fracture model for characterizing the tensile behavior of 2d woven composites. *Composite Structures* 204, 536–547.
- Zhou, X.Y., Gosling, P.D., Pearce, C.J., Ullah, Z., Kaczmarczyk, K., 2016. Perturbation-based stochastic multi-scale computational homogenization method for woven textile composites. *International Journal of Solids and Structures* 80, 368–380.

Zhu, Q., Shao, J., Kondo, D., 2011. A micromechanics-based thermodynamic formulation of isotropic damage with unilateral and friction effects. *European Journal of Mechanics - A/Solids* 30, 316–325.